Aus der

Berufsgenossenschaftlichen Unfallklinik

Klinik für Unfall- und Wiederherstellungschirurgie an der
Universität Tübingen

The establishment of finite element models to characterize mechanical properties of mouse tibiae based on micro-CT data

Inaugural-Dissertation
zur Erlangung des Doktorgrades
der Medizin

der Medizinischen Fakultät
der Eberhard Karls Universität
zu Tübingen

vorgelegt von

Huang, Xiaowei

2023

Dekan:	Professor Dr. B. Pichler
1. Berichterstatter	Professor Dr. A. Nüssler
2. Berichterstatter:	Professor Dr. C. Thiel

Tag der Disputation: 03.05.2023

To my grandfather

Table of contents

List of abbreviations

BV/TV	Bone volume density
BMD	Bone mineral density
BS/BV	Bone surface area density
CAD	Computer-assisted design
CBCT	Cone-beam computed tomography
Ct. Th.	Cortical wall thickness
DICOM	Digital Imaging and Communications in Medicine
DA	Degree of Anisotropy
FEA	Finite element analysis
FE	Finite element
HR-pQCT	High-Resolution Peripheral Quantitative Computed Tomography
IGES	The Initial Graphics Exchange Specification
KO	Knock out
MRI	Magnetic resonance imaging
μFEA	Micro-finite element analysis
micro-CT	Micro-computed tomography
PYD	Post-yield displacement
SMI	Structure Model Index
STL	Stereolithography
SAMP6	Senescence-accelerated mouse prone 6
Tb. Th.	Trabecular thickness
Tb. Sp.	Trabecular space
Tb. N.	Trabecular bone number
Tb. Pf.	Trabecular pattern factor
3R	Reduce Refine Replace
TLR	Toll-like receptor
ROI	Regions of interest

1. Introduction

1.1. Overview of bone structure

Bones are hard tissues in or on the body of an organism. For humans, bones are in the body, which is called the endoskeleton (Atake and Eames, 2021). For animals such as arthropods, mollusks, and some vertebrates (such as fish and reptiles), bones cover the body surface, called the exoskeleton (Afanassieva, 2021). In medical research, bones usually refer to the endoskeleton of humans or vertebrates and are the main structures that support the body, allow movement, and protect internal organs (Montoya *et al*., 2021), as illustrated in Figure 1.

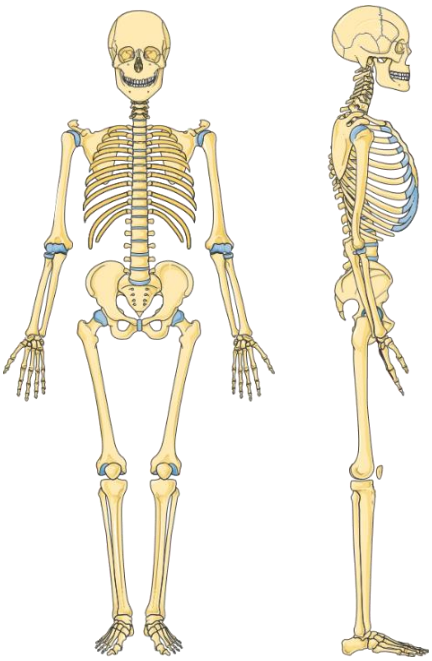

Figure 1. An illustration of the human skeleton. The front view (left) and the side view (right) of the human skeleton. The image was generated with Servier Medical Art (https://smart.servier.com/).

1.1.1. The macroscopic structure of bone

Bone comprises cortical and cancellous parts. Cortical bone is a dense bone tissue with low porosity (approximately 5%–10%) that constitutes the diaphysis and metaphyseal shell of long bones (Loundagin and Cooper, 2022). Cancellous bone is comprised of rod-shaped trabeculae and plate-shaped trabeculae connected as a network. It is mainly

located in the distal metaphysis of long bones, vertebral bodies, and skulls. It has a high rate of porosity, usually 60%–90% (Viero *et al.*, 2022). Trabecular bone porosity can change with age, and an increase in bone porosity associated with massive bone loss is commonly found in postmenopausal women after the age of 50 years (Zhang *et al.*, 2022a). Li *et al.* (2019) analyzed the aging-related changes in the female condylar bone mineral density (BMD) and trabecular structure by cone-beam computed tomography (CBCT). They found that, with increasing age, the female condylar bone volume decreases, the trabecular number (Tb. N.) and trabecular thickness (Tb. Th.) decrease, trabecular spacing (Tb. Sp.) increases, and plate-like trabecular bone gradually transforms into a rod-like form. These changes are most apparent in postmenopausal women compared with men and fertile women (Li *et al.*, 2019).

1.1.2. The microstructure of bone

Microscopically, bone is composed of cortical and cancellous bone, as shown in Figure 2. Cortical bone comprises numerous osteons at the microstructural level. Cancellous bone is composed of trabeculae with beam-like structures. Mechanical stimulation greatly influences bone growth, and bone trabeculae are aligned along the principal stress direction (Barbe *et al.*, 2022).

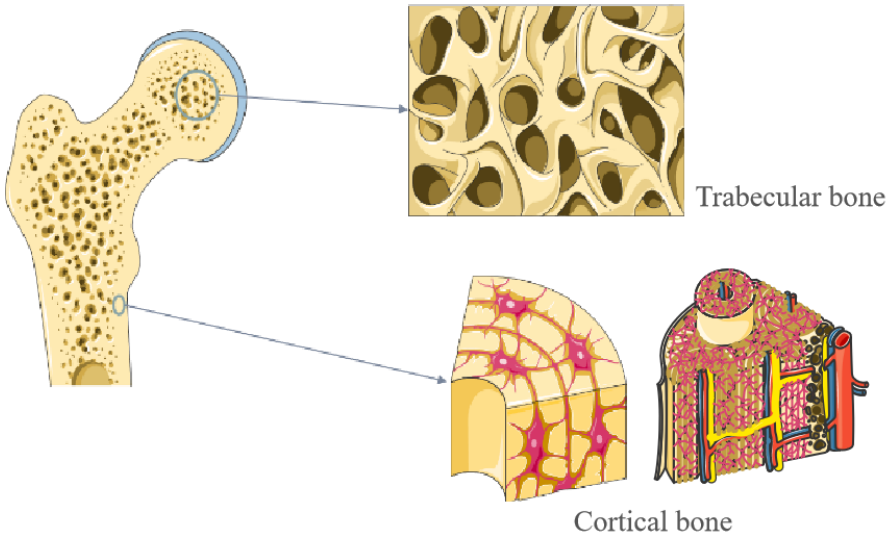

Figure 2. The microstructure of the proximal femur. It is composed of two distinct parts, cortical and cancellous components. Cancellous bone is composed of interconnected beam-like structures. Cortical bone is composed of osteons. The image was generated with the assistance of

Servier Medical Art (https://smart.servier.com/).

1.1.3. Bone remodeling and adaptation to changing external loading patterns

Bone remodeling plays a vital role in bone metabolism. Bone changes caused by bone remodeling activities mainly include changes in bone density, geometry, and mechanical properties (Feng and McDonald, 2011; Hadjidakis and Androulakis, 2006). Parfitt (1979) proposed that bone remodeling is a self-replacement mechanism of mature skeletal tissue, which can effectively prevent the accumulation of bone fatigue damage and maintain its mechanical properties. The famous Wolff's law states that changes in external loading patterns lead to changes within the structure of the bone tissue (Frost, 2001, 2004). More specifically, changes in the external force exerted on the bone induce directional bone remodeling. As shown in Figure 3, bone remodeling happens through the entire life cycle of an organism, with almost 100% of the skeleton being renewed during the first year of life and approximately 10% every year in adulthood (Schapira and Schapira, 1992).

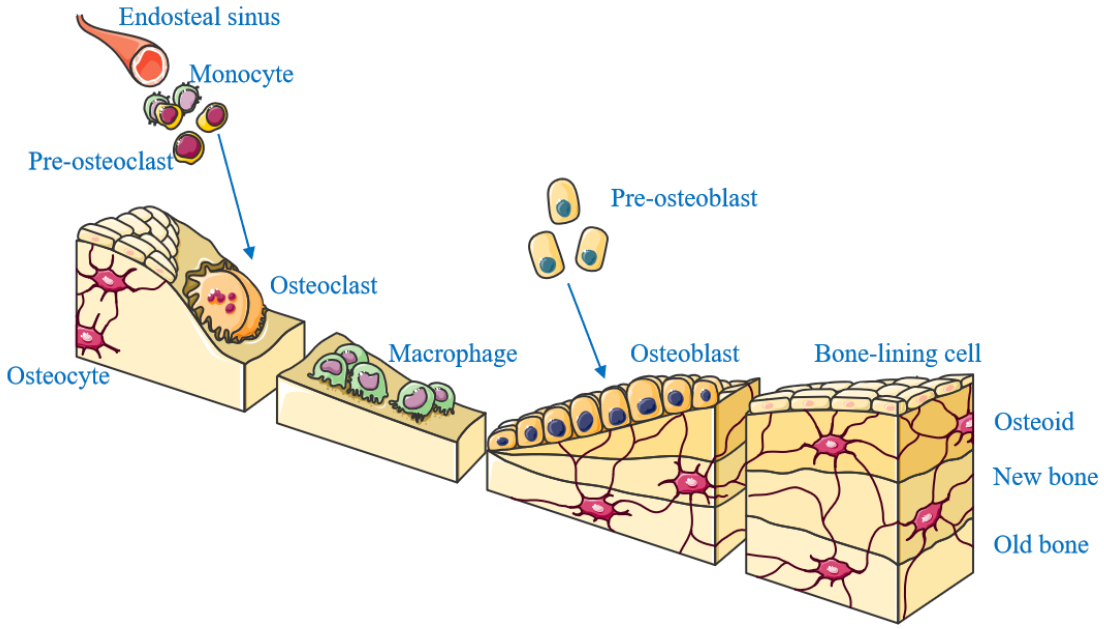

Figure 3. The bone remodeling process. Bone remodeling is a complicated process involving multiple cells. Osteoclasts remove and resorb old bone, while osteoblasts contribute to the mineralization of new bone. The image was generated with the assistance of Servier Medical Art (https://smart.servier.com/).

1.1.4. Bone mechanics is still a topic of interest

As biology, anatomy, and clinical medicine have developed, there has been a profound

increase in the understanding of bones, and significant progress has been made in diagnosing and treating bone-related diseases (Khalaf *et al.*, 2022; Shanmugavadivu *et al.*, 2022). However, there are still many unknown issues in bone mechanics, that is, the changes in mechanical properties during bone growth, development, and degeneration (Cole and van der Meulen, 2011; Grassi and Isaksson, 2015). Bone and cartilage differ from other engineering materials (Yang *et al.*, 2022). The most significant difference is that bone constantly undergoes complex physical and chemical changes in coordination with the life activities of organisms (Sharir *et al.*, 2008). Pure biological or mechanical research has been unable to explore the properties of bone materials in a satisfactory manner. The rise of interdisciplinary biomechanics has shown the potential to deepen research on bone materials (Sanz-Herrera *et al.*, 2021; Vaananen *et al.*, 2019).

Biomechanical parameters of long bones are determined by biomechanical measurements. In long bones, physiological loading usually involves bending and torsion (Burr *et al.*, 1996; Fritton *et al.*, 2000). A notable consideration when choosing between bending and torsional testing is that intact long bones tend to fail in a brittle manner during torsional compared with bending testing (Silva *et al.*, 2006). Therefore, a bending test is recommended if the perturbation is expected to alter bone ductility (Jepsen *et al.*, 2015). Bending stiffness is a critical parameter that can be measured directly by a material testing machine in a three-point bending setup. This approach can be used to characterize the biomechanical properties of the whole tibia, as shown in Figure 4, because it can characterize the elastic phase of material behavior (Brodt *et al.*, 1999). More specifically, it measures the amount of elastic deformation experienced by a structure when loaded. The term “elastic” means that applying low loading levels (*e.g.*, as experienced during physiological loading) does not damage the material, such that the bone returns to its original state when unloaded. For a given load, stiffer structures are expected to experience less tissue-level deformation under physiological loading. The stiffness of

bones depends on cortical morphology and material properties (Jepsen *et al.*, 2015).

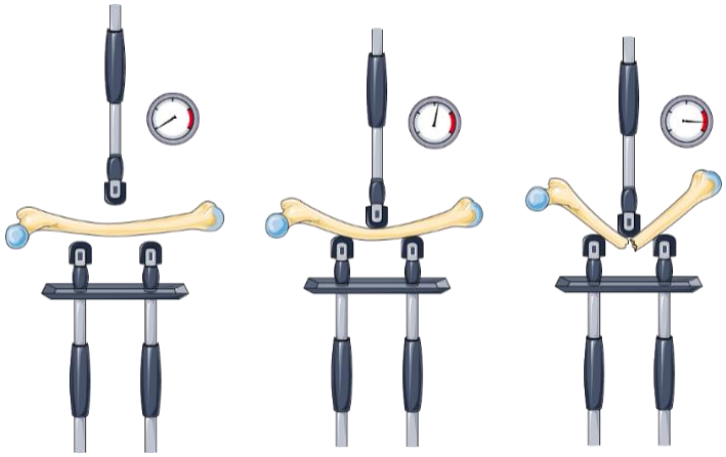

Figure 4. An illustration of the three-point bending setup. The bone is placed on the two supporters, and loading force is inflicted on the middle of the bone. The image was generated with the assistance of Servier Medical Art (https://smart.servier.com/).

1.2. Characterizing bone morphology using micro-computed tomography

Characterizing morphological parameters in bone during the life cycle is one of the focuses of bone remodeling research. Several imaging methods have been developed to visualize bone microstructure in three dimensions (3D) (Guha *et al.*, 2022; Zhang *et al.*, 2022b). The most widely used method in basic science and clinical research is micro-computed tomography (micro-CT) (Viero *et al.*, 2022). This method can capture grayscale images of the bone from multiple perspectives (Neldam and Pinholt, 2014). In this way, micro-CT technology provides precise 3D images of bone structure, allowing an accurate assessment of 3D microstructural features of cancellous and cortical bone (Rowe *et al.*, 2018). Muller *et al.* (1998) studied cylindrical iliac bone samples dissected from 63 patients. They first scanned the samples with micro-CT, embedded them with methyl methacrylate, and obtained two-dimensional (2D) images using non-demineralized bone slices. They compared the conventional methods with 3D micro-CT scanners in terms of bone volume density (bone volume divided by total volume, BV/TV), bone surface area density (bone surface area divided by bone volume, BS/BV), Tb. Th., and Tb. Sp. They found little difference between the 3D and 2D images, indicating that micro-CT is a fast, accurate, and non-destructive inspection method to determine the

internal structure of the sample. The 3D bone structure imaging technology of micro-CT can also be used to scan live animals, revealing the 3D structural characteristics of bones in a noninvasive manner (Ghavami-Lahiji *et al.*, 2021).

1.2.1 Two types of micro-CT machines

Existing micro-CT systems are designed in two configurations, one for *ex vivo* imaging (sample rotation) and another for *in vivo* imaging (X-ray system rotation). Micro-CT systems for *ex vivo* imaging are generally designed to have a spatial resolution close to tissue microscopy (Muller *et al.*, 1998). They require a micro-focus X-ray tube, usually with two to four times geometric magnification. The merit of this design is that it can provide 3D connectivity, topology, and microstructure of the complete sample, with a resolution ranging from 15 to 50 μm, and a field of view ranging from 15 to 50 mm. As *ex vivo* micro-CT is a noninvasive method, the sample's integrity will not be affected in subsequent histological analyses (Barbier *et al.*, 1999).

Micro-CT systems for *in vivo* imaging are primarily used in small animals (such as rodents) (Ning *et al.*, 2022). The above-mentioned principles of *ex vivo* imaging are also applicable to *in vivo* imaging. For *in vivo* micro-CT imaging, a rotating gantry system (carrying a source and a 2D detector) is required, with the consequence of a slightly lower resolution, generally 50–100 μm. Higher-resolution imaging requires high doses of whole-body X-ray radiation that animals cannot tolerate. Lowering the solution allows for decreased magnification, an enlarged field of view, and reduced exposure times. For anesthetized animals, shortening the exposure time interval can produce high-quality images and reduce the artifacts caused by heart and lung movement (Kinney *et al.*, 1995; Paulus *et al.*, 2001).

1.2.2. Characterizing trabecular bone based on micro-CT data

The main feature of cancellous bone is its porous structure. The trabecular structure in different parts of cancellous bone varies greatly depending on the anatomical site and the

type of bone (Zioupos *et al.*, 2008). In the past, most structural parameters describing cancellous bone had been analyzed with single-layer histological sections using special scanning software (Stevens and Latorraca, 1977). Analysis of these histological sections mostly provided 2D data. However, histomorphometric or patterned 2D methods cannot accurately reflect the 3D microstructure of trabecular bone (Compston and Croucher, 1991). The application of micro-CT technology perfectly solves the above-mentioned problems and has been widely used to study cancellous bone (Kohler *et al.*, 2021). It can analyze the 3D structure of the specimen, providing data on the 3D microstructure of trabecular bone while preserving the integrity of the specimen (Chappard *et al.*, 2008). The main parameters that can be measured based on micro-CT data are listed in Table 1.

Table 1. Measurement of trabecular parameters based on micro-CT data.

Parameters	Definition and units of parameters
Bone Volume, BV	Trabecular bone volume in the region of interest, in mm^3.
Total Volume, TV	The total volume of the region of interest, in mm^3.
Volume Fraction (BV/TV)	The ratio of trabecular bone volume to total volume.
Bone surface, BS	Trabecular bone surface area within the region of interest, in mm^2.
Surface area density (BS/BV)	The total area in a unit volume, in mm^{-1}.
Trabecular thickness (Tb. Th.)	The average thickness of the beam structure of trabecular bone in the region of interest, in mm.
Trabecular bone Separation (Tb. Sp.)	The average distance between beam structures, in mm. As the value increases, the distance increases, and the mechanical performance of the region of interest decreases.
Trabecular bone Number (Tb. N.)	The number of intersections between beam elements and non-beam structures, in mm^{-1}.
Structure Model Index (SMI)	The composition of the trabecular bone plate and columnar trabecular bone. When bone lesions occur, the plate trabecular bone decreases, the columnar bone trabecula increases, and the number of SMI increases.
Connectivity (Conn)	Interconnection of the beam structure in mm^{-3}.

1.3. The concept of finite element analysis

Finite element analysis (FEA) is a method belonging to the category of computational mechanics. The basic idea is to simulate, calculate, analyze, and predict the properties of a whole complex entity with the combined properties of a finite number of simple decomposed units (Schileo and Taddei, 2021), as shown in Figure 5. This method was first applied to calculate structural mechanics in industrial fields such as aircraft manufacturing and has been rapidly improved with the development of engineering, mathematics, and computer technology (Fadiji *et al.*, 2021; Vurtur Badarinath *et al.*, 2021). Its application has been extended to the biomechanics of living organisms (Lewis *et al.*, 2021; Naoum *et al.*, 2021). The primary characteristic of FEA is to decompose objects into simple elements. The typical workflow includes: discretizing the whole entity, adding a calculation formula, establishing a stiffness matrix, and solving outcome parameters such as stress and strain (Schileo and Taddei, 2021).

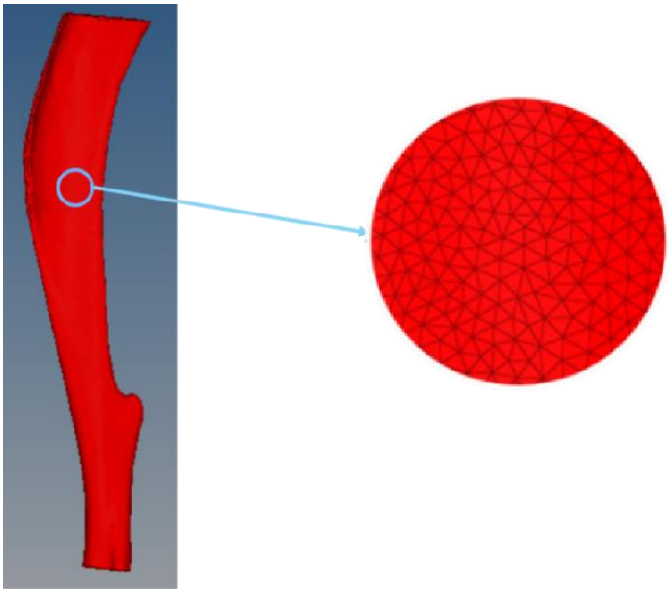

Figure 5. Decomposition of a mouse tibia model into a considerable number of tetrahedral elements. The small triangles are facets of the elements. After calculating the entire model, the outcome parameters such as the stress and strain of each elements can be computed and visualized for further analysis. The figure was created by the author.

1.3.1. Application of FEA in bone research: history and trend

The history of applying computational biomechanics to bone can be traced back to an

accidental collaboration between German engineer Culmann and the Swiss anatomist von Meyer. In 1866, Culmann discovered that his crane stress diagram was similar to von Meyer's chart of the trabecular bone structure in the proximal femur (Culmann, 1866). This discovery attracted attention, and the German medical scientist Wolff conducted in-depth research and proposed the famous Wolff's law of trabecular arrangement in 1892 (Wolff, 1892). In 1917, Koch began applying simple beam theory to analyze the stress distribution of the femur, thus starting the development of computational bone biomechanics (Koch, 1917). Later, Turner *et al.* (1965) successfully used FEA to calculate the stress and deformation of the shell-type structures from aircraft. Because FEA can successfully simulate and calculate the mechanical characteristics of complex elastic bodies, some scholars have tried to apply it in the medical field and have achieved success. In 1972, FEA was first reported to successfully analyze the biomechanical properties of bone (Brekelmans *et al.*, 1972). Normally, the stress and displacement pattern can be calculated and visualized, as illustrated in Figure 6. Its application has gradually expanded to the biomechanical simulation of bones of the whole body and even trabecular bone (Chen *et al.*, 2022; Goyal and Prasad, 2022; Li *et al.*, 2022b; Mercan *et al.*, 2022).

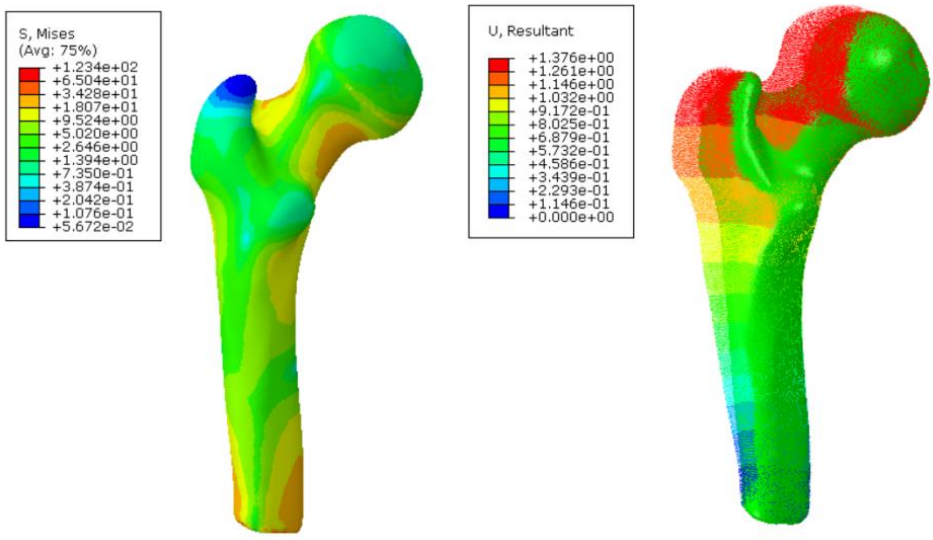

Figure 6. Visualization of FEA calculation. The distal part of the femur was fixed with loading on the femur head to mimic the physiological loading condition. The left part is the stress nephogram, and the right part is the displacement nephogram. Different colors indicate the distribution of outcome values. The stress is concentrated on the femur neck. The displacement

increases gradually from the distal end to the proximal femur head. The figure was created by the author.

After nearly 40 years of application and development in orthopedics-related basic and clinical research, FE technology has continued to progress and has made outstanding achievements in improving simulation performance (Lewis *et al.*, 2021; Prados-Privado *et al.*, 2020). The FE model has evolved from the original simple and rough 2D data model to a highly complex and realistic 3D model (Behforootan *et al.*, 2017; Feyzi *et al.*, 2021). The number of elements included in the model increases exponentially, and the simulation accuracy improves accordingly (Donahue *et al.*, 2002). The material assignment strategy has developed from a single homogeneous material to heterogeneous multi-property materials (Schwarzenberg and Dailey, 2020; Xin *et al.*, 2013); from isotropic materials to anisotropic materials (Castillo-Mendez and Ortiz, 2022; Ding *et al.*, 2022); and from simple homogeneous structures to the inclusion of tissue structures, *e.g.*, cortical bone and cancellous bone, articular cartilage, the bone marrow cavity, ligament, muscle, and even soft tissue such as the joint capsule (Jaecques *et al.*, 2004; Li *et al.*, 2022a; Luo *et al.*, 2022). Several applications of FEA in orthopedic surgery research are listed in Table 2.

Table 2. The application of FEA in orthopedic surgery research.

Authors	Studies
Belytschko *et al.*, 1974	Using FEA to analyze intervertebral discs' biomechanical properties as early as 1974 (Belytschko *et al.*, 1974).
van Rietbergen *et al.*, 2002	Three-dimensional FEA simulation was used to predict the mechanical characteristics of cervical vertebral burst fracture, obtained with good simulation and repeatability (van Rietbergen *et al.*, 2002).
Schileo and Taddei, 2021	The early two-dimensional plane model has been replaced by a three-dimensional model (Schileo and Taddei, 2021).
Lewis *et al.*, 2021	The type of analysis has evolved from simple stress analysis to the exploration of the mechanism of fracture patterns and other pathogenesis of bone-related diseases (Lewis *et al.*, 2021).

Harrigan *et al.*, 1992	The first attempt to use CT-scanned data to establish a FE model of the proximal femur (Harrigan *et al.*, 1992).
McNamara *et al.*, 1997	Created 3D FE models for an artificial joint after hip replacement. The stress distribution on the interface between bone and prosthesis has been measured with satisfactory consistency with the results of traditional mechanical experiments (McNamara *et al.*, 1997).
Vichnin and Batterman, 1986	FEA to analyze the impact of the thickness of the bone cement on joint replacement in terms of the posterior femoral stress distribution to determine the optimal volume of bone cement for prosthesis fixation (Vichnin and Batterman, 1986).
Rogge *et al.*, 2002	3D FEA to compare the biomechanical properties of different internal fixation methods (Rogge *et al.*, 2002).
Gefen and Seliktar, 2004	FEA to verify Wolff's law for the first time on the calcaneus. Three-dimensional FE models of the calcaneus were established and used to calculate the direction of stress conduction in the calcaneus in a standing position. The generated data were compared with calcaneal anatomical specimen slides (Gefen and Seliktar, 2004).

1.3.2. The concept of micro-finite element analysis

Micro-finite element analysis (μFEA) is FEA for studying microstructures. Its emergence is inseparable from the continuous progress of high-resolution image scanning technology and computer software and hardware technology (Macneil and Boyd, 2008). Since 1973—when CT scanning was first reported to be clinically applied—the resolution of CT scanning has advanced from the order of centimeters to the sub-millimeter level, and the resolution of micro-CT has even reached micrometer resolution (San-Julian *et al.*, 1999). These technological breakthroughs have allowed microscale examination of trabecular bone. Thanks to the breakthrough in imaging techniques, 3D reconstruction of the bone microstructure and μFEA are now possible, and μFEA based on micro-CT data has been regarded as the gold standard for the non-destructive study of bone microstructure (Herblum *et al.*, 2013). In 2008, Macneil and Boyd (2008) reported the application of high-resolution peripheral quantitative computed tomography (HR-qQCT) to characterize the microstructure of the human distal radius. The authors performed

μFEA on the scanned images and confirmed that μFEA with suitable boundary conditions can accurately simulate and calculate the biomechanical characteristics of the distal radius (Macneil and Boyd, 2008).

Besides, high-resolution magnetic resonance imaging (MRI) has been employed to characterize the microstructure of bone. Rajapakse *et al.* (2010) recently reported the use of high-resolution MRI (160 μm) to acquire micro-CT images of the distal tibia *in vivo*. The scanned data were analyzed by μFEA and compared with the results of μFEA based on *ex vivo* micro-CT data. They found that both can accurately simulate and calculate the biomechanical characteristics of the distal tibia. van Rietbergen *et al.* (2002) also reported the application of high-resolution MRI to analyze the calcaneus of postmenopausal women with osteoporosis. They did not detect significant changes in bone mass, but the simulated biomechanical indexes showed substantial changes. Thus, they described a new approach for the early detection of osteoporosis. Pistoia *et al.* (2002) constructed an FEA model containing 2 million elements with high-resolution images obtained from high-resolution CT scans. They found that the simulated results based on FEA demonstrated a good correlation with the actual measured results ($p < 0.001$, $R^2 = 0.75$). As computer software and hardware technology continue to advance, μFEA, based on a large amount of data from microscale imaging, has shown broad application prospects to reconstruct and simulate the microstructure of bone.

1.4. Mouse as a popular experimental animal in bone research: a potential target for FE simulation

Rodents are widely used in animal experiments, with rats and mice accounting for more than 50% of skeletal studies (Huss *et al.*, 2019). The laboratory mouse (*Mus musculus*) is the animal model most commonly used to study physiology and disease at the cellular, molecular, and genetic levels because of its short gestation period of only 3 weeks, high reproductive capacity, and easy genetic manipulation.

There are two typical examples of the application of mice for osteoporosis-related *in vivo* studies. Senescence-accelerated mouse prone 6 (SAMP6) is an accelerated aging mouse strain. It is the only spontaneous animal model that has been proved to develop fragility fractures with age. Of note, there are no significant differences between males and females. It is a suitable model to study senile osteoporosis. Recent morphological and molecular studies of SAMP6 mice have shown that cancellous bone is significantly lost, but the cortical bone does not change significantly during the aging process (Makida *et al.*, 2020). Besides, the formation of new bone on the endosteal surface is reduced, and the fat tissue in the bone marrow cavity is increased (Makida *et al.*, 2020). The other specific example of research on age-related osteoporosis is with ovariectomized mice, which can simulate the bone quality changes of aged women after menopause. In addition, mice fed a high-fat diet can also be used to simulate the pathological condition of diabetes-related osteodystrophy (Kau *et al.*, 2011).

1.4.1. Laboratory animals and animal welfare

Laboratory animals are indispensable in biomedical research (Green, 2015). For example, preclinical evaluation of interventions and numerous studies of pathogenic mechanisms are performed using animal models (Hartung, 2013). Our understanding of the underlying mechanism of biological systems, such as the skeletal and cardiovascular systems, is often based on findings from *in vivo* studies. Pharmaceutical interventions are tested for efficacy and safety in animals before moving on to clinical trials in humans (Carbone and Austin, 2016). Currently, more than 100 million animals are euthanized each year for biomedical experiments (Taylor and Alvarez, 2019).

In 1959, the British zoologist Russell and the microbiologist Burch published the book *The Principles of Humanitarian Experimental Technology*, in which they put forward the 3R principle. This concept refers explicitly to the necessity to replace, reduce, and refine the use of experimental animals (Manciocco *et al.*, 2009). According to the explanation in the book, replacement refers to the use of non-living material to replace living animals.

Reduction refers to minimizing the number of animals used based on the expected quantity and accuracy of the obtained information. Refinement refers to avoiding any unnecessary harm or distress inflicted on experimental animals (Richmond, 2002). The 3R principle has aroused public attention to alternative methods to animal experiments. Some specialized research institutions and foundations have been established to advocate the 3R principle in education and research. Since the 1980s, the 3R principle has become the theoretical basis for animal welfare legislation and animal research ethics in many countries (Neuhaus, 2020). Indeed, the accepted ethical standards for the supervision and monitoring of animal experiments are inspired by Russell and Burch's 3R principle. Many researchers now explore alternative techniques to fulfill the 3R principle.

1.4.2. The application of μFEA to simulate mice bone mechanics

As long as the use of laboratory animals is still inevitable, the prerequisite for public acceptance is to understand that it will cause minor pain to the smallest number of animals and that humans and other animals can benefit from their sacrifice (Diaz *et al.*, 2020). FEA can simulate the complexity of various materials and is suitable for solving models of complex boundary conditions (Varga *et al.*, 2020). The general steps of FEA are illustrated in Figure 7. Therefore, using μFEA for simulation could be a promising method for the mechanical characterization of bones to minimize the number of mice used for biomechanical study, which fits well with the 3R principle.

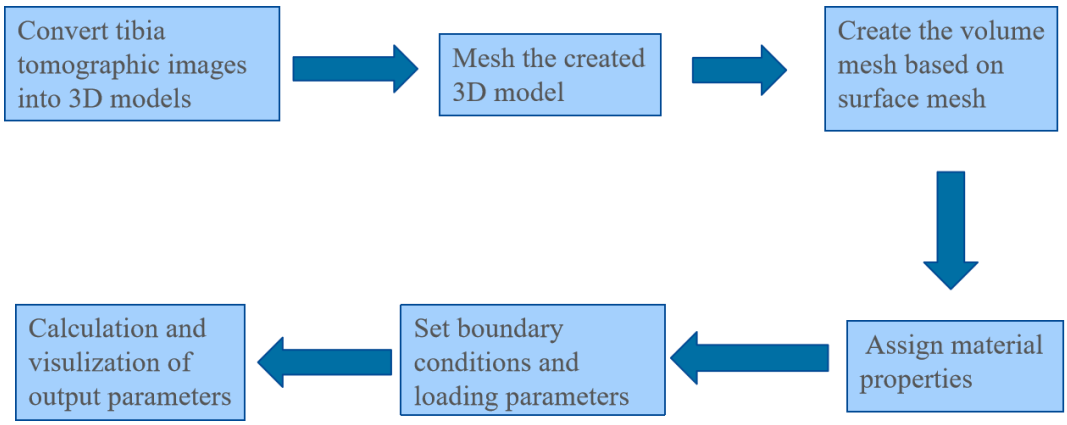

Figure 7. Flow chart of μFEA of mouse tibia. There are six main steps. The first step is to generate 3D geometric models. The next four steps are to convert the geometric models to FE models. The last step is to calculate the outcome parameters, such as stress. The distribution of

the outcome parameters can be displayed by nephograms as shown in Figure 6. The figure was created by the author.

2. Aim of the research

The research objective was to establish and validate three FE models based on micro-CT data of mouse tibia to minimize the use of mice in biomechanical experiments. To achieve this goal, the following points were addressed:

- Establish two FE models with axial loading and comparison of different material assignment methods in terms of simulation accuracy.
  - Validate the axial loading FE models by correlating the calculated parameters with morphological and experimental parameters.
- Establish the three-point bending FE model and compare different material assignment methods in terms of simulation accuracy.
  - Validate the model by comparing bending stiffness calculated based on FEA with bending stiffness measured experimentally.

3. Materials and methods

3.1. Mouse tibia

The micro-CT data and biomechanical parameters of TLR knockout mice were part of Elena Gneiting's bachelor's thesis (Gneiting, 2017). C3H/HeN wild-type mice were used as a control group. C3H/HeJ mice exhibit TLR4 deficiency (TLR4-def) and endotoxin resistance (Hoshino *et al.*, 1999), and thus they were used as TLR4 knockout mice. TLR2/4 knockout mice were established based on the C3H/HeJ background with TLR2 knockout (Sartorius *et al.*, 2012). Mice from each of the three genotypes were randomly assigned to the high-fat diet (Harlan Laboratories, Madison, WI, USA) or standard rodent chow group, as shown in Figure 8. For the high-fat diet, 45% of the calories came from fat (lard), and 36% of total fat was saturated fatty acids (Kau *et al.*, 2011). After sacrificing

mice at an average age of 12 weeks, both hind limbs were cut off in the middle of the femur and frozen at -80°C until further examination.

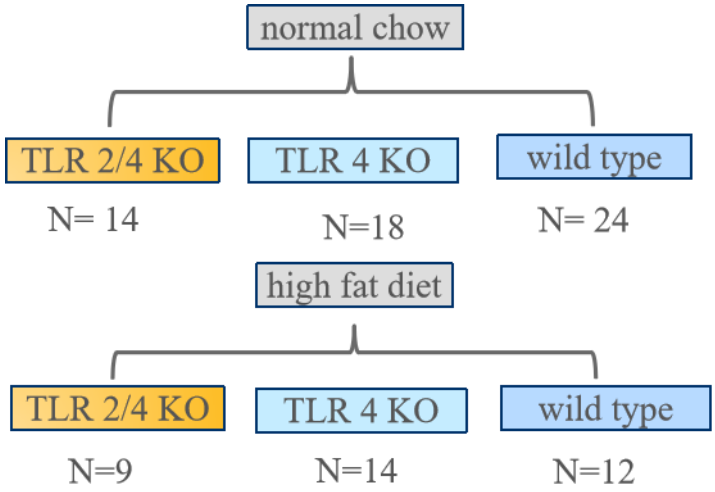

Figure 8. An illustration of the experimental groups and sample sizes of TLR knockout mice. N indicates the sample size of each subgroup.

The micro-CT data and biomechanical parameters of WISP1 knockout mice were part of Ingo Seiler's bachelor's thesis. The wild-type and WISP1 knockout lines were bred based on the C57BL/6 strain (Seiler, 2017). The WISP1 gene is highly expressed by osteoblasts and their precursors. It can regulate the proliferation of osteocytes through the PI3K/Akt/GSK-3β pathway (Maiese, 2022). Fifteen mouse tibiae, including eight tibiae from wild-type mice and seven tibiae from WISP1 knockout mice, were extracted with the attached fibula and disconnected from the paw and femur. After the bones were cleaned of the remaining soft tissue, they were frozen at -80°C until further examination (Schwartz *et al.*, 2011).

3.2. Micro-CT scanning

The aforementioned tibia were placed in a 2 mL tube filled with water and examined with a micro-CT scanner (micro-CT 80, SCANCO MEDICAL, Switzerland) with an exposure time of 1000 ms (Huang *et al.*, 2022). The scan resolution voxel size was 35 µm, based on a previously described collection and analysis method (Kau *et al.*, 2011). The obtained micro-CT datasets were saved in the Digital Imaging and Communications in Medicine (DICOM) format (Huang *et al.*, 2022).

3.3. Characterization of morphological parameters of mouse tibia

From the CT scans, a fixed cube volume (dimensions: 0.823 × 0.588 × 0.49 mm, 0.237 mm^3) was selected to evaluate the trabecular bone parameters. This cube was located at the height of the tibia and fibula connection. To distinguish between bone tissue and bone marrow in the cube, the threshold was set to 650 mg hydroxyapatite (HA)/cm^3. The results included BV/TV, BS/BV, Tb. Th., Tb. N., Tb. Sp., and Tb. Pf.. To evaluate the average cortical wall thickness (Ct. Th.), eight concentrically arranged cortical wall distance measurements were made on a half-length axial section of each tibia, as illustrated in Figure 9.

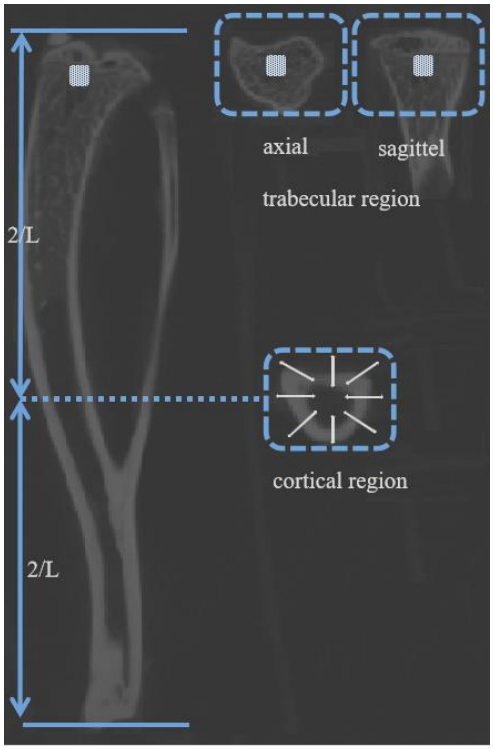

Figure 9. An illustration of the morphological parameters measured. The white blocks were used to mark the region of interest (ROI) to characterize trabecular bone. Eight concentrically arranged cortical wall distance measurements (white lines) were made on a half-length axial section of each tibia. The cortical wall thickness is the mean value of the eight measurements.

3.4. Whole bone mechanical property measurement

The biomechanical strength of the tibia was calculated using load-displacement curves acquired from a three-point bending load frame (Zwicki Z2.5 TN, Zwick Roell, Ulm, Germany). During the trial, the tibia was in a state of compression on the back and tension on the front. The anterior surface was placed on two lower supports, 10 mm apart (60%

of the average tibia length). The speed of compression was 0.025 mm/s. The load-displacement curves were measured until failure. The parameters include ultimate load (N), stiffness (N/mm), work to fracture (Nmm), and post-yield displacement (mm). The yield point was defined as the intersection of the load-displacement curve and the 90% slope of the stiffness (Jepsen *et al.*, 2015).

3.5 FE model creation

Table 3. The list of software packages used and their roles in the present study.

Software used	Function
Mimics 20.0 software (Materialise NV., Leuven, Belgium)	Establishment of the 3D geometric model of mouse tibia; material assignment
3-Matic 12.0 software (Materialise NV., Leuven, Belgium)	2D re-meshing
Geomagic studio 2012 software (3D Systems, Rock Hill, SC, USA)	3D geometric model modification
Hypermesh 14.0 software (Altair Engineering, Troy, USA)	Finite element preprocessing
ABAQUS 6.14 software (Simulia Inc., Providence, USA)	Finite element model calculation and visualization
Solidworks 2019 software (Solidworks, Massachusetts, USA)	Creating a 3D geometric model of cylinders

3.5.1. Micro-CT data importation

The micro-CT datasets of mouse tibia were stored in the DICOM format and then imported into Mimics software (Materialise NV., Leuven, Belgium) for further processing. This program is a comprehensive medical information processing software that is widely used for 3D printing, digital medicine, computer-aided design (CAD), and FEA, among others (Zhu *et al.*, 2022). It can process CT scan data and create 3D models.

In the present study, all the DICOM images with the suffix dcm should be selected, as demonstrated in Figure 10, and imported into Mimics software.

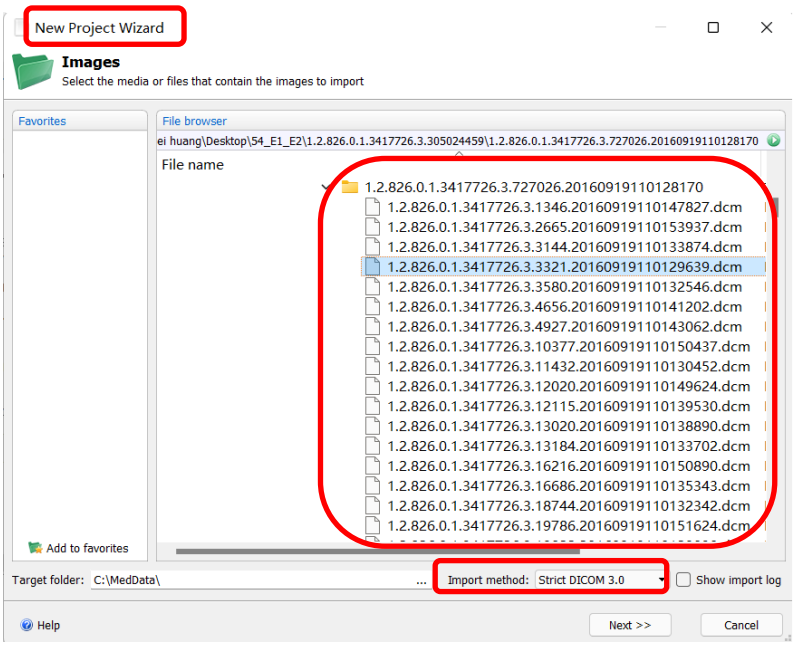

Figure 10. Import of micro-CT data. Open the pathway of stored micro-CT data through the New Project Wizard modulus. All the slides of micro-CT data should be selected. The import method was chosen as Strict DICOM 3.0.

After importing the raw DICOM data, the images of three different views can be viewed simultaneously, as shown in Figure 11.

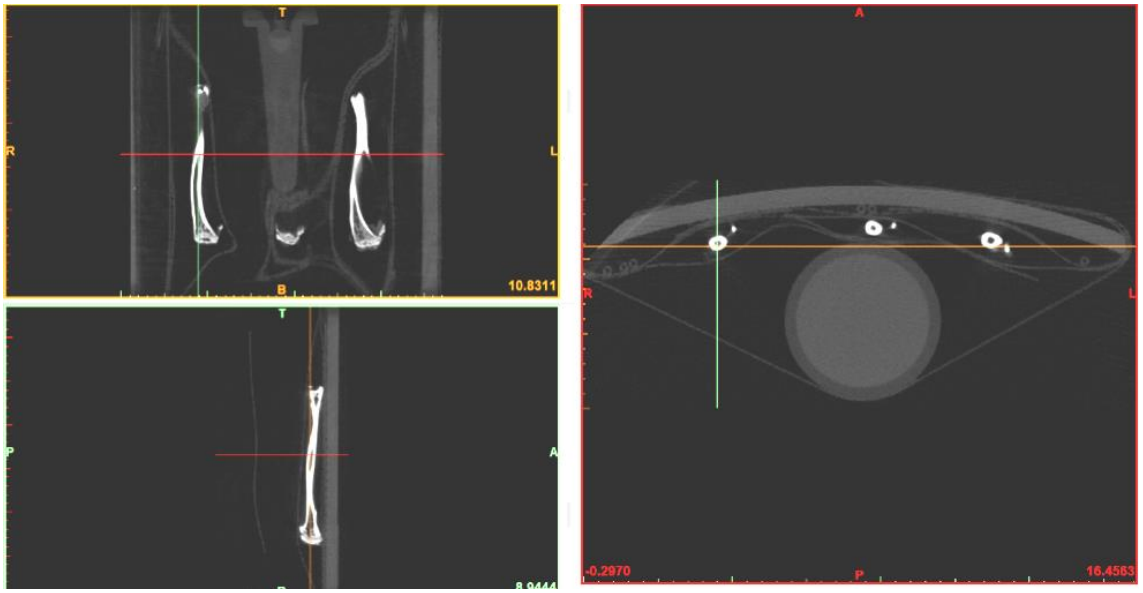

Figure 11. After the import process, sagittal, coronal, and horizontal views of the tibia (three mouse tibiae) can be shown in Mimics software. The upper left part is the coronal view of three mouse tibiae. The lower left part is the sagittal view of the bones. The right part is the horizontal

view of the three bones.

3.5.2. Extraction of the tibia image from the micro-CT data

The Hounsfield unit (HU) value is positively correlated with tissue density. Generally, the HU value of bone tissue ranges from 700 to 3000 (De Vos *et al.*, 2009). In the present study, HU values > 1100 was chosen to select the bony part of the scanned tibia, as shown in Figure 12.

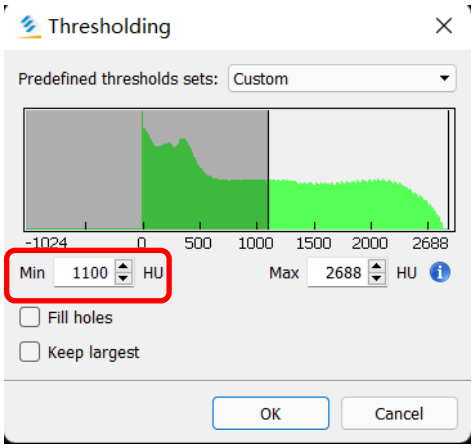

Figure 12. The function window for thresholding. A HU value ranging from 1100 to 2688 (maximal value in the micro-CT data set) was chosen to select the bone material of the scanned tibia.

Through thresholding, the micro-CT data of the bony part of the tibia was highlighted with green, as illustrated in Figure 13B. The specific part of the tibia was picked using the regional growing function and marked with blue, as shown in Figure 13C.

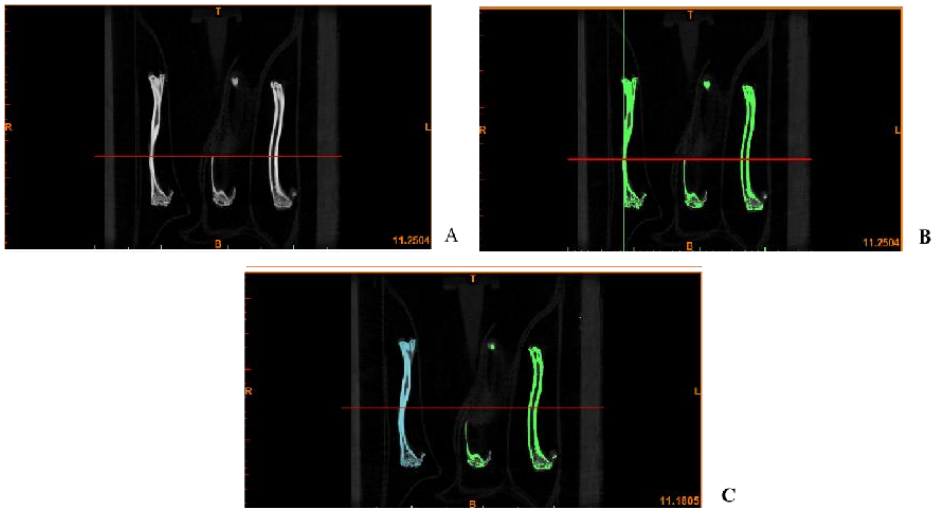

Figure 13. Selection of the bony part of the tibia for 3D reconstruction. After the thresholding

procedure, the bony part from whole tibia scanning (A) was highlighted with green color (B). Region growing function was used to select the specific bone (cyan) from the three bones (green) for 3D reconstruction (C).

3.5.3. Creating 3D models based on micro-CT data

3D models of the mouse tibiae were created using the calculate part function, with reconstruction quality chosen as optimal, as shown in Figure 14. After completing reconstruction, the 3D geometric model was saved in the stereolithography (STL) format for the following procedure. The reconstruction quality was chosen as optimal, as it can create the optimized model based on the resolution of raw data.

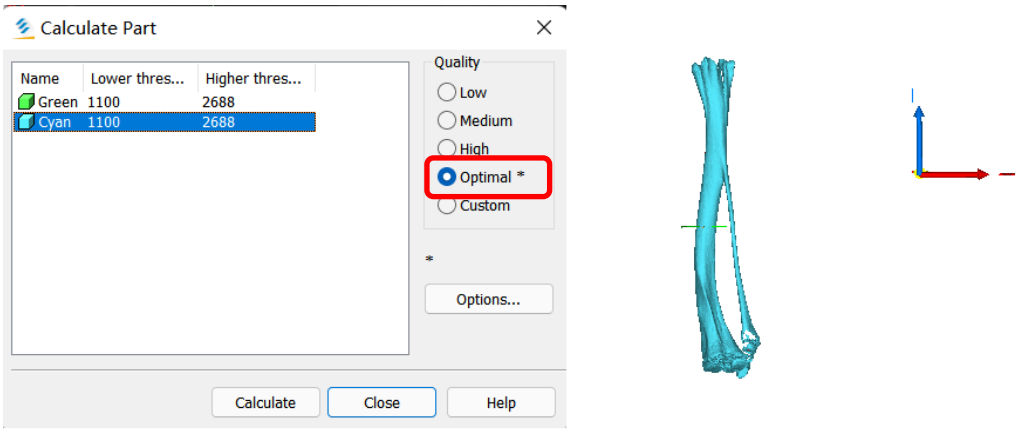

Figure 14. Calculation of chosen bone scans to build the 3D model. In the function window (left), the specific bone material (cyan) was chosen for reconstruction. After completing the reconstruction, the 3D geometric model was established (right).

3.5.4. Creation of a cylinder with a diameter of 2 mm using Solidworks software

A 3D geometric cylinder was created using the Solidworks software (Solidworks, Waltham, MA, USA). First, a circle with a diameter of 2 mm was created in the sketch section. Next, the extrude function in the features section was used to create the cylinder, as shown in Figure 15. The 3D geometric model of the cylinder was saved in the Initial Graphics Exchange Specification (IGES) format and then imported into Geomagic Studio software (3D Systems, Rock Hill, SC, USA) for model assembly.

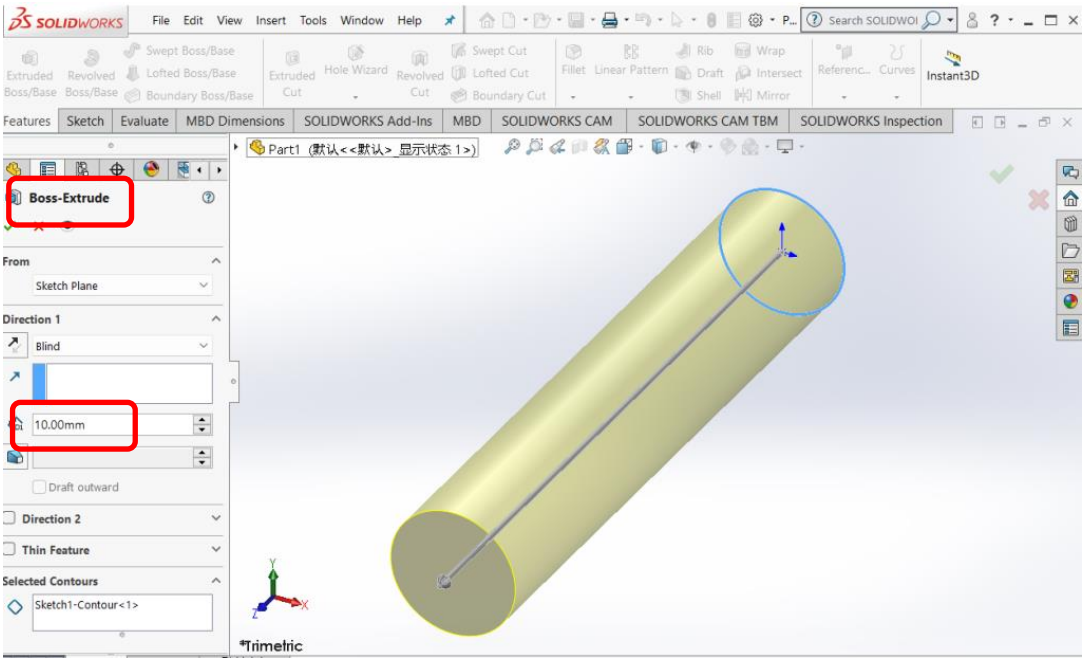

Figure 15. Creation of cylinders with diameters of 2 mm using Solidworks software. The cylinder was created with Solidworks software. First, a circle with a diameter of 2 mm was created. Then, the boss-extrude function was used to generate a cylinder based on the circle. The length of the cylinder was set as 10 mm.

3.5.5. 3D model polishing and assembly

The constructed 3D models were saved in the STL format and imported to Geomagic Studio software that was designed for reverse engineering (Xu *et al.*, 2022). In this step, the processing function of the polygon stage model in the Geomagic Studio software was used to modify and remove irregular shapes from the proximal femur model to facilitate volume meshing. The trimming function was used to remove the distal and proximal ends of the tibiae to facilitate boundary condition setting, as shown in Figure 16.

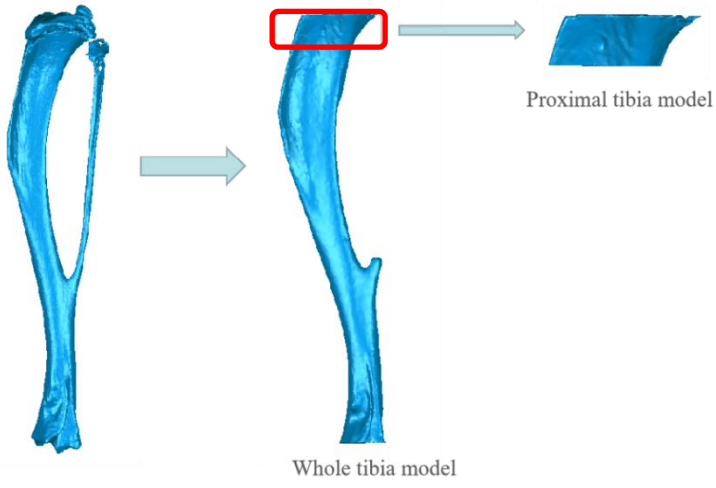

Figure 16. The 3D geometric model of the whole tibia model and the proximal tibia model. The upper part above the tibia-fibula junction and the lower part below the tibia-fibula junction were removed. The proximal part with 10% of the whole tibial length was extracted as the proximal tibia model.

The modified model was also saved in the STL format. For the three-point bending setup simulation, the cylinder created previously was assembled with the 3D geometric tibia model setting, as shown in Figure 17. The cylinder was used to inflict loading on the bone.

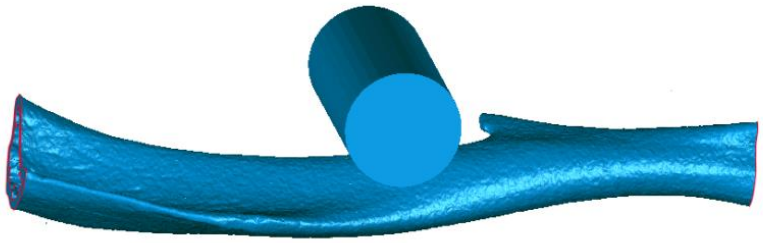

Figure 17. The 3D geometric model to simulate a three-point bending setup. The cylinder and the tibia were assembled using Geomagic Studio software. The cylinder was placed above the middle of the tibia to be used for loading transmission.

3.5.6. 2D element re-meshing

The STL file exported from Geomagic studio software was imported to 3-Matic software (Materialise NV). 3-Matic software is a module of the Mimics software and is mainly used for mesh modification. 3-Matic software has been primarily used for 2D shell element refinement and re-meshing (Milheiro *et al.*, 2022). The uniform mesh function was used to re-mesh the 2D meshes automatically generated in Mimics software and to generate evenly distributed 2D meshes with the same size specified, as shown in Figure 18. After completing re-meshing, the models were saved and exported in the STL format.

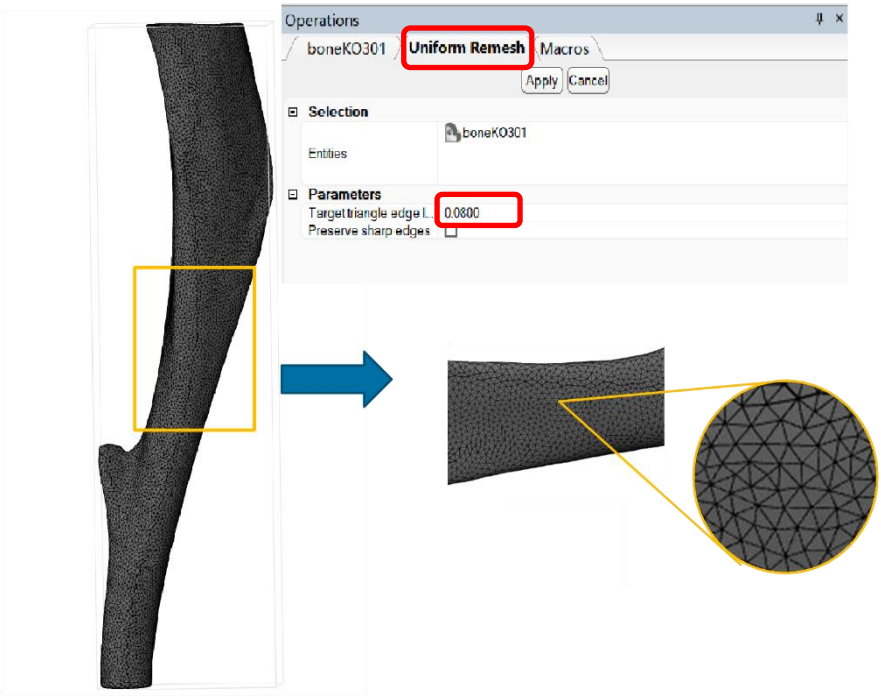

Figure 18. The meshing of 2D elements of mouse tibia. The uniform remesh function was used to set the mesh size of the bone model as 0.08 mm. The mesh size indicated the length of the triangles. In this case, the length of all triangle sides was set as 0.08 mm.

3.5.7. Creating 3D volume elements

Hypermesh is a preprocessing software integrated into HyperWorks (Altair Engineering, Troy, MI, USA) (Foletti *et al.*, 2019). Its FE preprocessing function includes FE meshing and geometric modification. In addition, it has different interfaces to connect with the CAD software and can import geometric files. It can also create pre-processing files for Abaqus 14.0 software (Simulia Inc., Providence, RI, USA) to generate inp files and directly import them into FE calculation software.

In the present study, the re-meshed 2D models were imported into Hypermesh software. The tetra mesh function was used to create 3D volume meshes based on the 2D meshes of the imported models, as shown in Figure 19. After completing volume meshing, the 2D meshes were deleted. The models were then exported to Mimics software for material assignment as inp files.

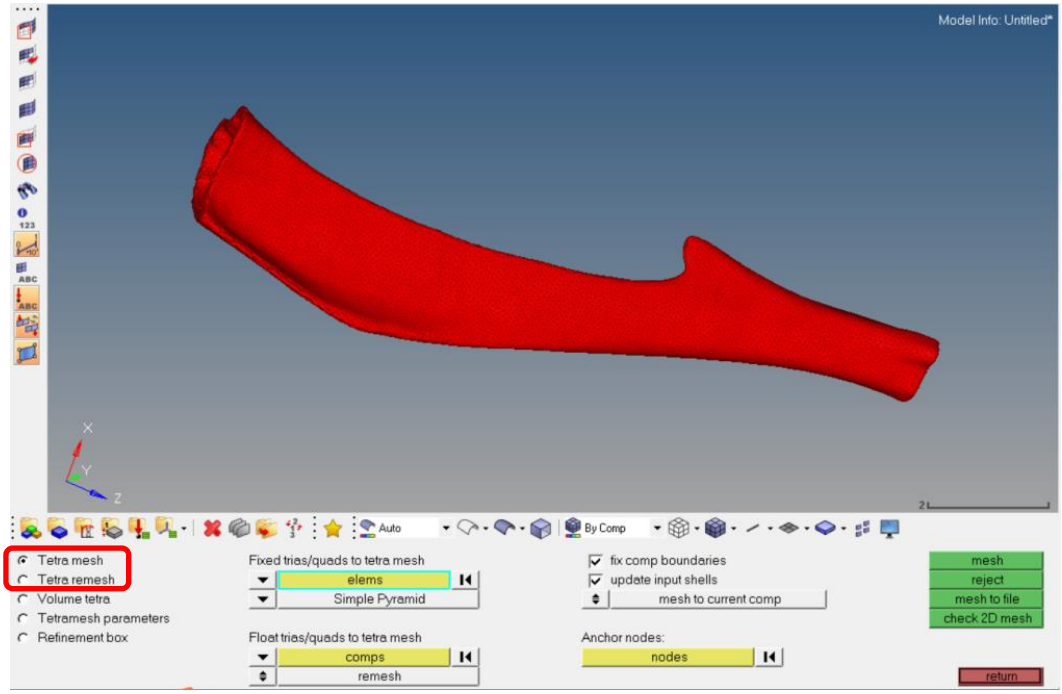

Figure 19. Creation of 3D elements based on 2D elements in Hypermesh software. The input model was composed of 2D elements. The 3D volume tetrahedral meshes were created using the tetra mesh function.

3.5.8. Heterogeneous material assignment for FE models with axial loading

The inp file generated from the previous step was then input to Mimics software again to assign the material property according to gray values from micro-CT images (presented as HU in Mimics software). For the TLR knockout mouse tibiae, the relation between density and HU ($\rho = 1 \times HU$) and the equation describing the density and elastic modulus relationship ($E = 7.136 \times \rho - 172.3$) were obtained from published studies (Kopperdahl *et al.*, 2002; Rho *et al.*, 1995).

3.5.9. Heterogeneous material assignment for FE models with three-point bending

For the WISP1 knockout mouse tibiae, the relationship between density and elastic modulus was predicted based on a calibration scan in which cubes with known densities were scanned to get the corresponding HU value. The equation to calculate density based on the HU value is: Density (ρ) = $0.206 \times HU - 13.13$ mg HA/cm^3. The equation of elastic modulus and density was obtained from Currey (1988): Young's modulus (E) = 0.1127

× $\rho^{1.746}$ MPa. Poisson's ratio was set as 0.3 (Cheong *et al.*, 2021), as shown in Figure 20.

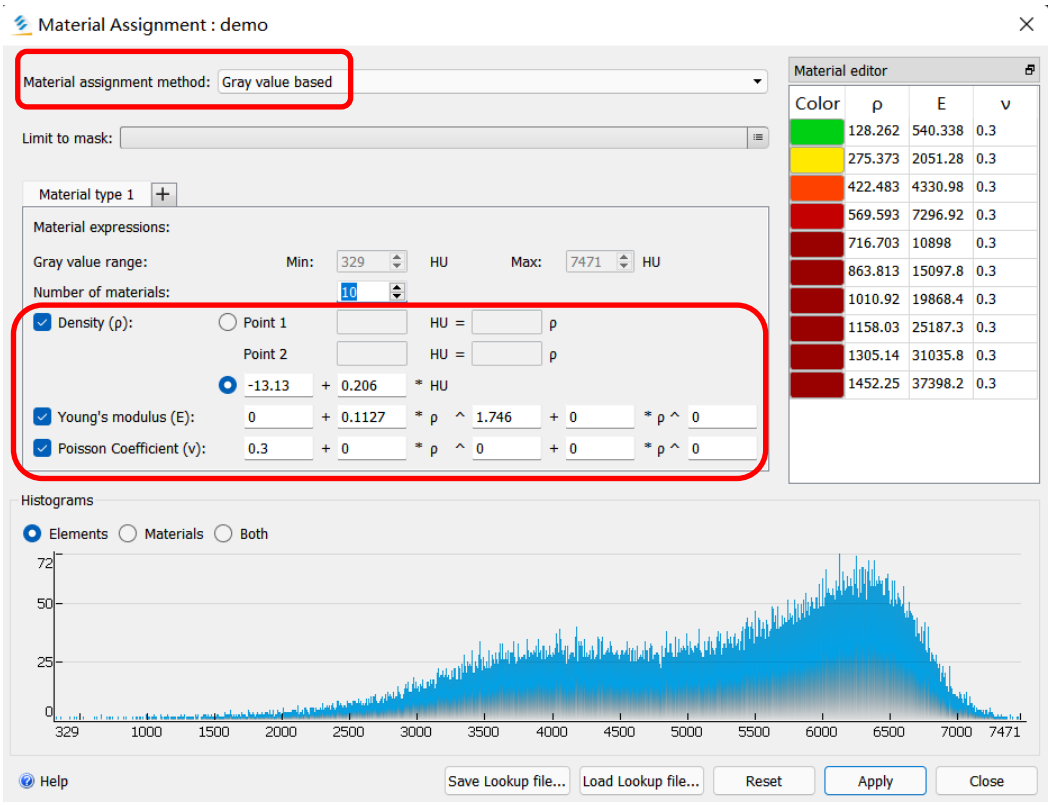

Figure 20. Heterogeneous material assignment using Mimics software. The material assignment method was chosen as the gray value-based assignment. Poisson's ratio was set as 0.3. The equation to calculate density based on the HU value is: Density (ρ) = 0.206 × HU – 13.13 mg HA/cm^3. The equation of elastic modulus and density is: Young's modulus (E) = 0.1127 × $\rho^{1.746}$ MPa. Histograms in the lower part of the figure show the distribution of HU values of the micro-CT data. The elastic modulus of bone was divided into 10 values depending on the density, as shown in the upper right part of the figure.

3.5.10. Boundary condition of axial loading models

For the whole tibia model, all nodes on the bottom surface of the bone were tied to one node (point b) outside the surface fixed at six degrees of freedom to immobilize the bottom of the whole tibia model. A downward displacement load of 5 μm was applied to the top node (point a) alongside the z-axis, as shown in Figure 21. Similarly, for the proximal model, the nodes on the inferior surface of the bone (point d) were fixed to immobilize the bottom of the proximal tibia, and a downward displacement of 5 μm was applied to the nodes on the top of the proximal surface (point c) alongside the z-axis, as shown in Figure 21.

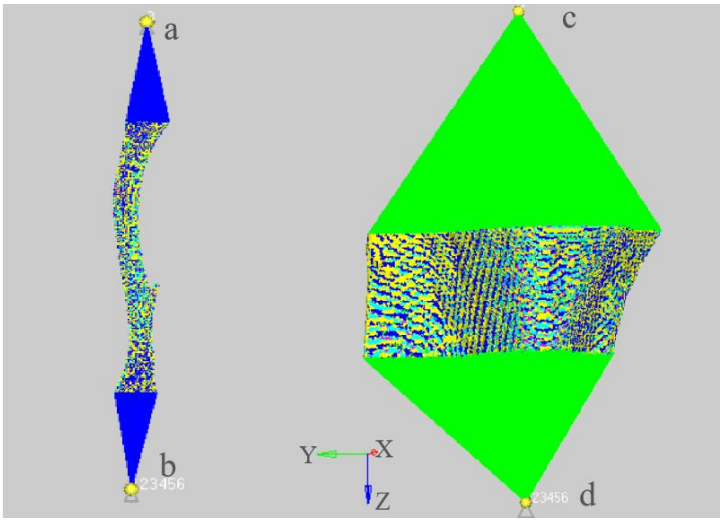

Figure 21. The boundary condition of the axial loading model. Points b and d are connected to the bottom surface of the tibia and were fixed at six degrees of freedom. The connection is marked with blue or green. The displacement load was then applied through points a and c along the direction of the z-axis.

3.5.11. Boundary condition of the three-point bending setup

As shown in Figure 22, the cylinder mentioned before was defined as a rigid body connecting to one point (point c) to inflict loading. Each supporting area was linked with two points. All degrees of freedom were constrained at the proximal point (point d). The distal end (point e) was allowed to move along the long axis of the tibia. A contact pair was created where the cylinder and the bone surface contact, with the friction coefficient set as zero.

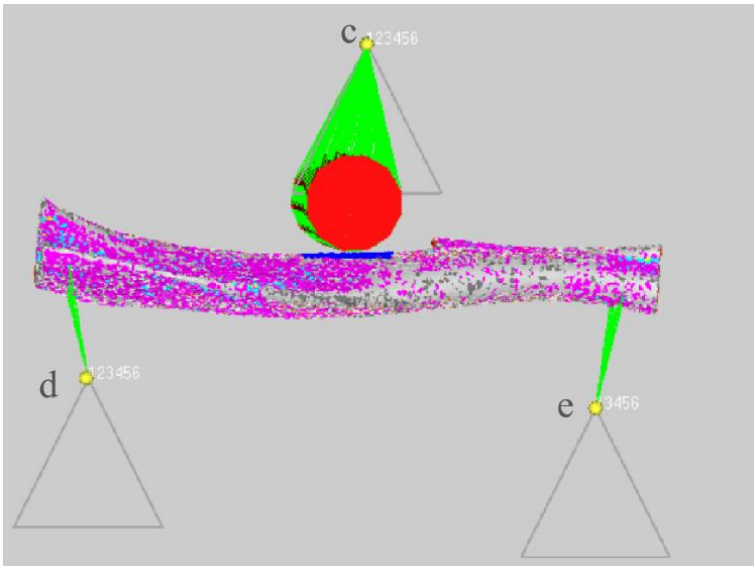

Figure 22. The boundary condition and three-point bending setup. Point d is the proximal point fixed at all degrees of freedom, and point e is the distal point fixed except for the direction alongside with long tibia axis. The displacement load was applied through point c to mimic a three-point bending setup.

3.5.12. Calculation and visualization of FE models with axial loading

In this stage, the inp file of the prepared FE models was loaded in Abaqus 14.0 software for final computation and post-processing. The axial stiffness of the bone structure was calculated as the reaction force of point a divided by the displacement of point a, as shown in Figure 23. The equation of axial stiffness is:

$$Axial\ \ stiffness = \frac{The\ \ reaction\ \ force\ \ of\ \ point\ \ a}{Displacement\ \ of\ \ point\ \ a}$$

The peak stress of the mid-shaft tibia is defined as the maximum stress on the cross-section of the axial tibia. The peak stress value was manually extracted from the cross-section of the mid-shaft tibia.

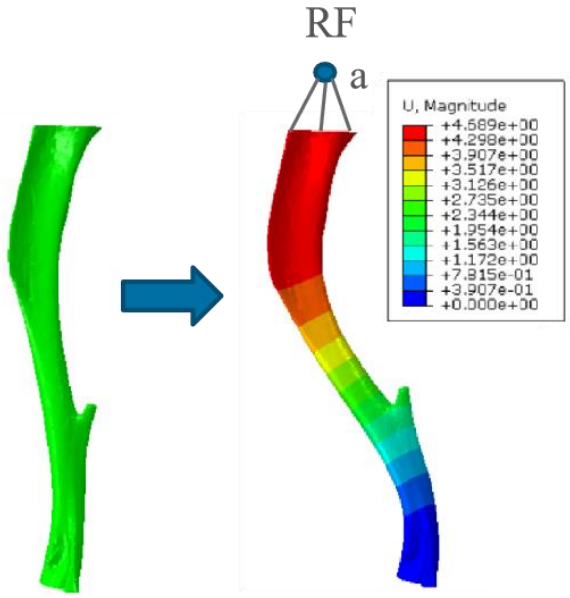

Figure 23. Deformation of mouse tibia after the axial loading. The displacement load was inflicted on point a. The proximal surface was connected to point a. The displacement and reaction force of point a was calculated in Abaqus 14.0 software.

3.5.13. Calculation and visualization of FE models with a three-point bending setup

Bending stiffness was calculated as the reaction force of point c divided by the maximal displacement of the tibia. The equation for bending stiffness is:

$$Bending\ \ stiffenss = \frac{The\ \ reaction\ \ force\ \ of\ \ point\ \ c}{Maximal\ \ displacement\ \ of\ \ the\ \ tibia}$$

The deformation of the mouse tibia after loading in a three-point bending setup was visualized in Abaqus 14.0 software, as shown in Figure 24.

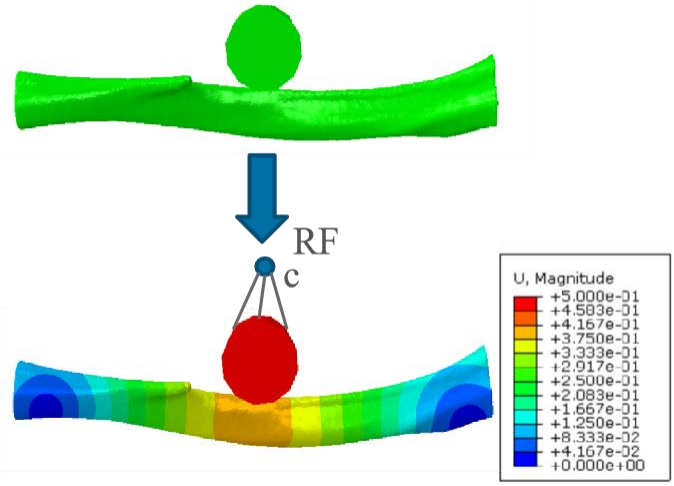

Figure 24. Deformation of mouse tibia after loading in a three-point bending setup. The displacement load was inflicted on point c. The reaction force of point c and the maximal displacement of the tibia were calculated in Abaqus 14.0 software.

3.5.14. Statistical analysis

To validate the FE models with axial loading, Pearson correlation analysis was used to examine the correlation between the morphological and mechanical parameters that were measured experimentally and calculated based on the FE models. To validate the FE models with a three-point bending setup, Pearson correlation analysis was conducted to analyze the correlation between bending stiffness that was measured experimentally and predicted by FEA. Besides, the experimentally measured and predicted bending stiffness was compared with the paired Mann–Whitney–Wilcoxon test. For all analyses, $p < 0.05$ was considered statistically significant.

4. Results

4.1. Calculation of three mechanical parameters based on two FE models with axial loading

Two types of FE models were generated based on the micro-CT scans of TLR knockout mice. The first model (Model A, Figure 25) is the whole tibia model with proximal axial loading. The axial stiffness of the entire tibia and peak stress of the mid-shaft tibia can be calculated based on this model. These two properties can be used to characterize the mechanical properties of the whole tibia. The second model (Model B, Figure 25) is the proximal tibia model similar to that reported by Heveran *et al.* (2019), which is the proximal part of the aforementioned whole tibia model. This model was used to calculate the stiffness of the proximal tibia, defined as proximal stiffness, to reflect the mechanical properties of trabecular bone.

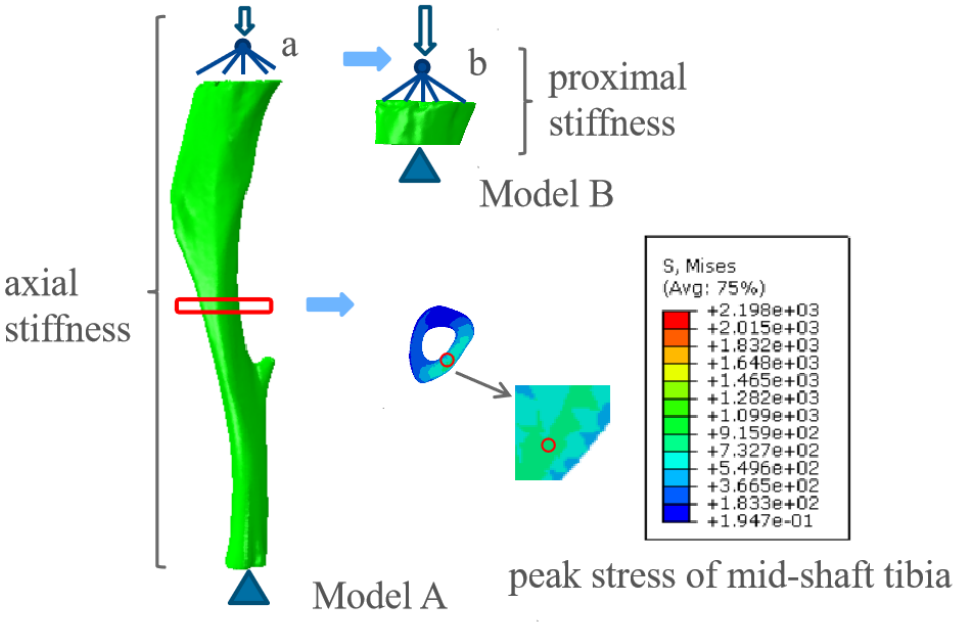

Figure 25. An illustration of two FE models with axial loading and the outcome parameters. Axial stiffness is calculated with the reaction force of point a divided by displacement of point a. Peak stress of the mid-shaft tibia is defined as the maximal stress in the mid-shaft cross-section of the whole tibia. Proximal stiffness is calculated by the reaction force of point b divided by the displacement of point b.

4.2. The choice of mesh size for the FE models with axial loading

Mesh size is believed to significantly affect bending stiffness (Liu *et al.*, 2020). Smaller mesh sizes can increase the accuracy of FE model simulation while also increasing the computing costs (increased computing time and higher demand for more advanced computer performance). The resolution of the micro-CT scan was 34.939 × 34.939 × 34.939 μm in pixel size (Gneiting, 2017), so the mesh size should be close to 0.035 mm. As a result, the mesh size of the whole tibia model was set as 0.04 mm. As the proximal tibia model is part of the entire tibia model and is much smaller in terms of the total number of elements, the mesh size of the proximal tibia model was set as 0.02 mm. The average number of elements and nodes of the whole tibia and the proximal tibia model are listed in Table 4.

Table 4. General information on the FE models with axial loading.

	whole tibia model	proximal tibia model
number of elements	890168±119560	541618±57590
number of nodes	117128±85632	65305±7125
size of mesh	0.04 mm	0.02 mm

4.3. The creation of FE models with fixed homogeneous material assignment

Heveran *et al.* (2019) set the bone material assignment as homogeneous, isotropic, and linear elastic (Young's modulus, E = 10 GPa, and Poisson's ratio, v = 0.3). The same material assignment strategy was applied for the two FE models with axial loading.

4.3.1. Correlation between mid-shaft peak stress and mechanical parameters

The peak stress of the mid-shaft tibia was calculated to characterize the biomechanical properties of the whole tibia. Pearson correlation analysis was utilized to examine the relationship between peak stress of the mid-shaft tibia and the whole bone–related mechanical parameters, namely bending stiffness, maximal load, post-yield displacement, and work to fracture. The correlations between peak stress of the mid-shaft tibia and

bending stiffness (p = 0.310, R^2 = 0.012), maximal load (p = 0.099 R^2 = 0.031), work to fracture (p = 0.115, R^2 = 0.029), and maximal displacement (p = 0.312, R^2 = 0.012) were not significant, as shown in Figure 26.

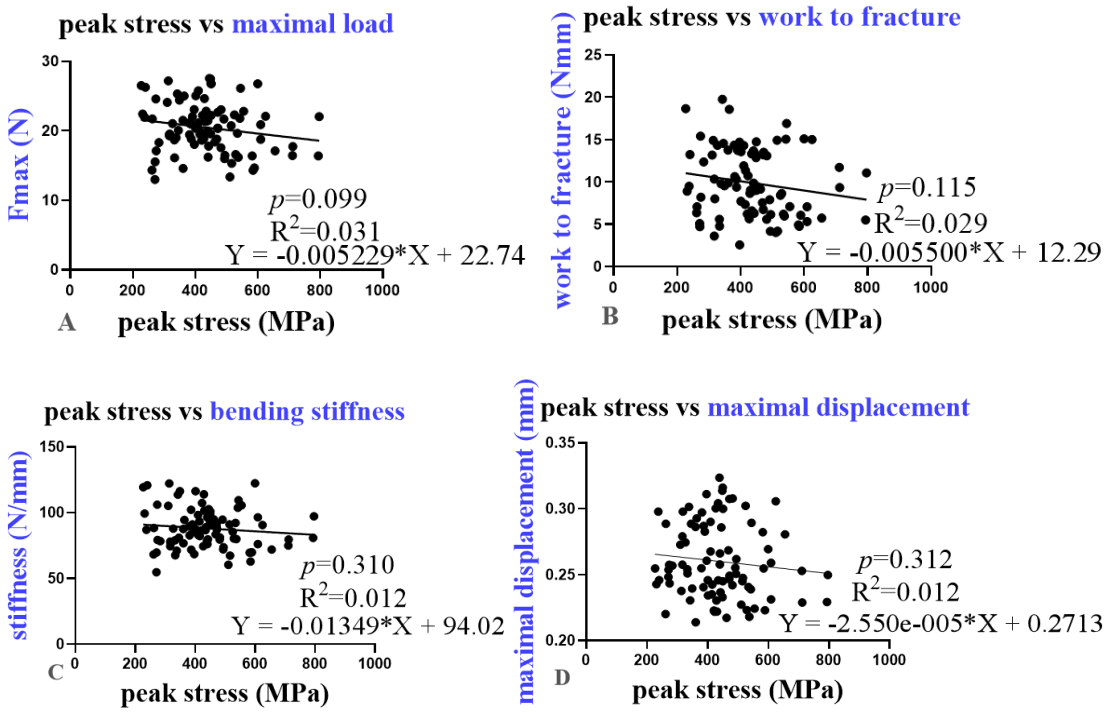

Figure 26. Correlation between peak stress and mechanical parameters. (A) Pearson correlation between peak stress and maximal load (p = 0.099, R^2 = 0.031). (B) Pearson correlation between peak stress and work to fracture (p = 0.115, R^2 = 0.029). (C) Pearson correlation between peak stress and bending stiffness (p = 0.310, R^2 = 0.012). (D) Pearson correlation analysis between peak stress and maximal displacement (p = 0.312, R^2 = 0.012). The sample size was 91.

4.3.2. Correlation between mid-shaft peak stress and cortical wall thickness

Peak stress was defined as the maximal stress in the middle section of the whole tibia. There was a negative correlation between peak stress and the mid-shaft cortical wall thickness (p = 0.014 and R^2 = 0.068), as shown in Figure 27.

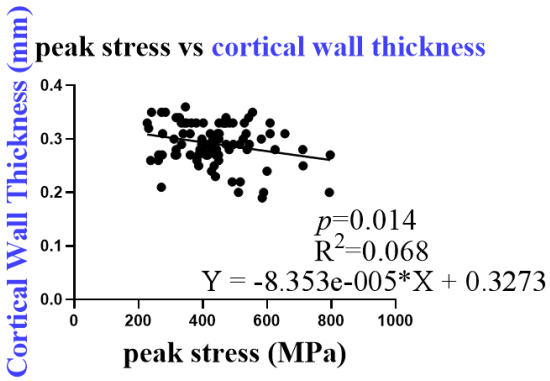

Figure 27. Correlation between peak stress and cortical wall thickness. There was a negative correlation between peak stress and the mid-shaft cortical wall thickness (p = 0.014, R^2 = 0.068). The sample size was 91.

4.3.3. Correlation between axial stiffness and mechanical parameters

Pearson correlation analysis was conducted to study correlations between axial stiffness and whole bone-related mechanical parameters, including bending stiffness, maximal load, post-yield displacement, maximal displacement, and work to fracture. The correlations between axial stiffness and bending stiffness (p = 0.889, R^2 = 0.000), maximal load (p = 0.604, R^2 = 0.003), work to fracture (p = 0.276, R^2 = 0.014), post-yield displacement (p = 0.188, R^2 = 0.020), and maximal displacement (p = 0.495, R^2 = 0.005) were not significant, as shown in Figure 28.

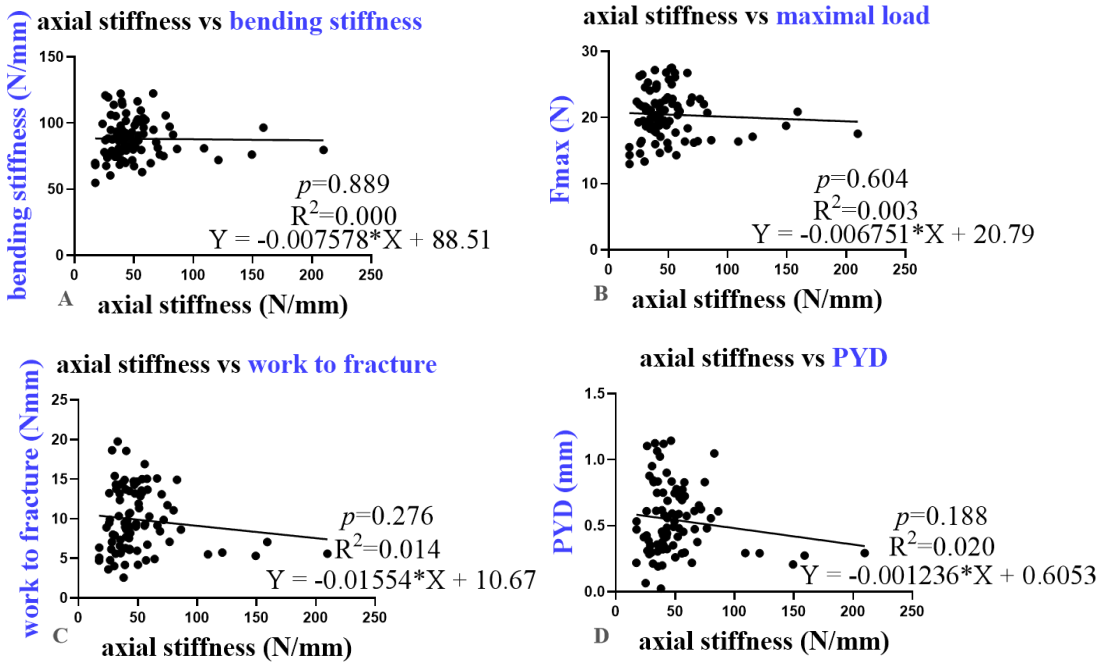

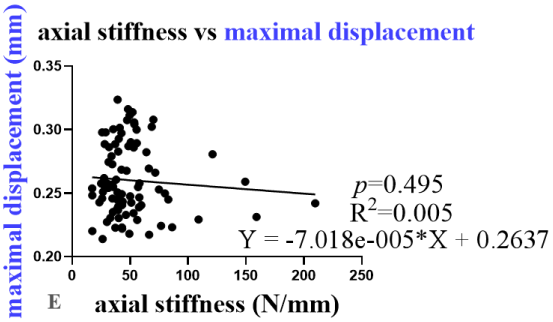

Figure 28. Correlation between axial stiffness and mechanical parameters. (A) Pearson correlation between axial stiffness and bending stiffness (p = 0.889, R^2 = 0.000). (B) Pearson correlation between axial stiffness and maximal load (p = 0.604, R^2 = 0.003). (C) Pearson correlation between axial stiffness and work to fracture (p = 0.276, R^2 = 0.014). (D) Pearson correlation between axial stiffness and post-yield displacement (p = 0.188, R^2 = 0.020). (E) Pearson correlation between proximal stiffness and maximal displacement (p = 0.495, R^2 = 0.005). The sample size was 91.

4.3.4. Correlation between proximal stiffness and trabecular morphological parameters

The stiffness of the proximal tibia (proximal stiffness) was calculated to characterize the biomechanical strength of the proximal part of the tibia, which is mostly composed of trabecular bone. Pearson correlation analysis was conducted to study the correlation between proximal stiffness and the measured morphological parameters, including BV/TV, BS/BV, Tb. Th., Tb. Pf., Tb. N., and Tb. Sp. The correlations between proximal stiffness and BV/TV (p = 0.481, R^2 = 0.006), BS/BV (p = 0.965, R^2 = 0.000), Tb. Th. (p = 0.947, R^2 = 0.000), Tb. Sp. (p = 0.132, R^2 = 0.027), Tb. Pf. (p = 0.833, R^2 = 0.001), and Tb. N. (p = 0.223, R^2 = 0.017) were not significant, as shown in Figure 29.

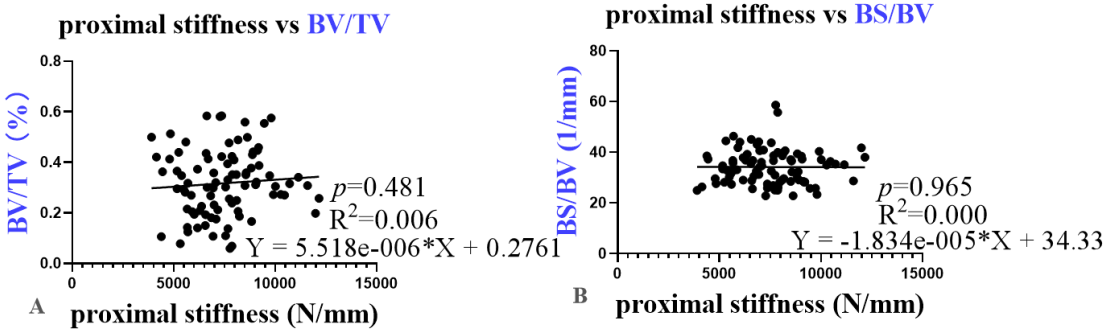

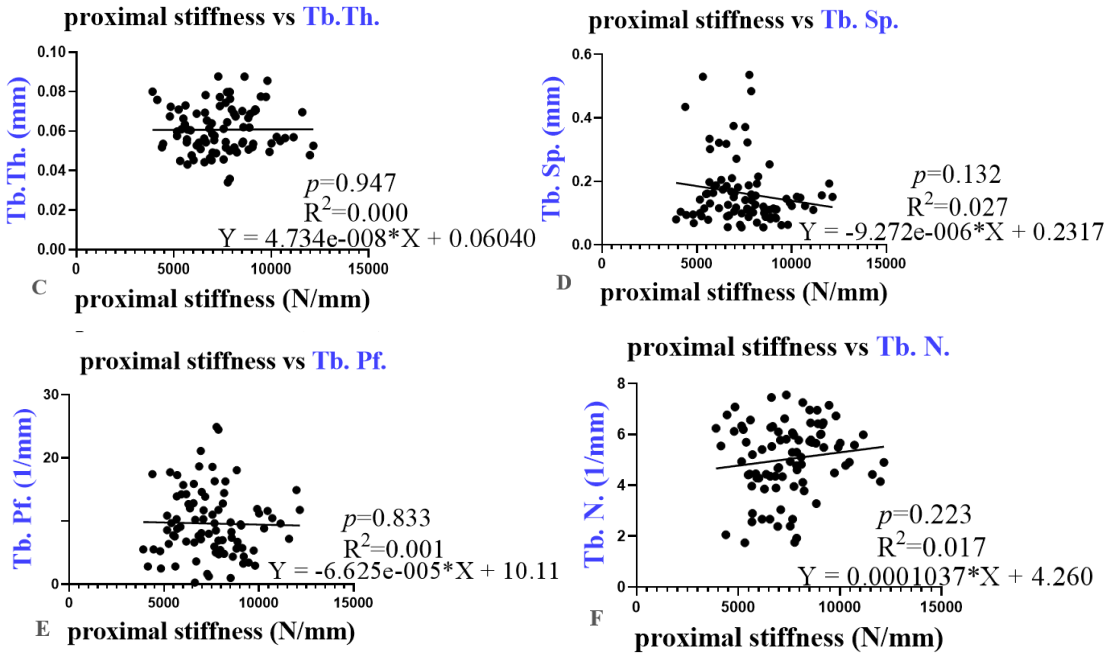

Figure 29. Correlation between proximal stiffness and trabecular morphological parameters. (A) Pearson correlation between proximal stiffness and BV/TV (p = 0.481, R^2 = 0.006). (B) Pearson correlation between proximal stiffness and BS/BV (p = 0.965, R^2 = 0.000). (C) Pearson correlation between proximal stiffness and the Tb. Th. (p = 0.947, R^2 = 0.000). (D) Pearson correlation between proximal stiffness and Tb. Sp. (p = 0.132, R^2 = 0.027). (E) Pearson correlation between proximal stiffness and Tb. Pf. (p = 0.833, R^2 = 0.001). (F) Pearson correlation between proximal stiffness and Tb. N. (p = 0.223, R^2 = 0.017). The sample size was 91.

4.4. Comparison of different equation combinations for gray value-based material assignment

The correlation results for the homogeneous material assignment method did not show a satisfactory correlation with the experimentally measured parameters. Consequently, the FE models were modified to provide better simulation. Material assignment plays an essential role in the accuracy of FE simulation. Heterogeneous material assignment is considered superior to homogeneous material assignment for more accurate simulation (Schwarzenberg and Dailey, 2020; Xin *et al.*, 2013). Therefore, a heterogeneous material assignment strategy based on the gray value distribution of the micro-CT scan was employed for the following simulations. Elastic moduli are typically defined by bone mineral density (BMD) and bone mineral density-modulus (E-BMD) equations derived from isolated compression tests of excised bone samples (Helgason *et al.*, 2008). The

relationship between density and gray value (expressed as the HU value in Mimics software) is defined by BMD equations. The correlation between Young's modulus and density was determined by E-BMD equations and obtained from previously published papers (Currey, 1988; Kopperdahl *et al.*, 2002; Perren, 1975), summarized in Table 5.

Table 5. The list of four combinations of the BMD equation and E-BMD equations.

BMD equation	E-BMD equation
ρ=1*HU	E=7.136*ρ-172.3
ρ=1.122*HU+47	E=2.20*ρ-209
ρ=1*HU	E=0.1127 $\rho^{1.746}$
ρ=1.122*HU+47	E=0.1127 $\rho^{1.746}$

To determine the optimal equation for simulation, the four aforementioned equation combinations were compared in terms of the elastic modulus range, as shown in Table 6. For the first equation combination, the elastic modulus ranged from 5637.4 to 16588.2 MPa, with a mean of 11212.8 MPa. For the second equation combination, the elastic modulus ranged from 18169.4 to 109167.0 MPa, with a mean of 58843.7 MPa. For the third equation combination, the elastic modulus ranged from 1904.0 to 5692.0 MPa, with a mean of 3789.0 MPa. For the last equation combination, the elastic modulus ranged from 13614.7 to 86576.2 MPa, with a mean of 46121.4 MPa. Based on the study by Heveran *et al.* (2019), the average Young's modulus of the proximal tibia is 10000 MPa. Hence, the first equation combination could be used as the potential option for material assignment, as the mean Young's modulus was 11212.8 MPa, the closest of the four combinations to 10000 MPa.

Table 6. The four equation combinations and the material parameter gradient generated. Density was calculated based on the HU value. Elastic modulus was calculated based on density. Based on the published literature, Poisson's ratio was set as 0.3 (Heveran *et al.*, 2019).

Combination 1		Combination 2	
BMD equation	E-BMD equation	BMD equation	E-BMD equation
$\rho=1*HU$	$E=7.136*\rho-172.3$	$\rho=1*HU$	$E=0.1127\rho^{1.746}$
ρ (mg HA/cm^3)	Elastic modulus (MPa)	ρ (mg HA/cm^3)	Elastic modulus (MPa)
814.1	5637.4	814.1	13614.7
984.7	6854.2	984.7	18975.7
1155.2	8070.9	1155.2	25078.4
1325.7	9287.7	1325.7	31893.2
1496.2	10504.5	1496.2	39395.5
1666.7	11721.2	1666.7	47564.5
1837.20	12938.0	1837.20	56382.2
2007.7	15154.7	2007.7	65832.5
2178.2	15371.5	2178.2	75901.4
2348.7	16588.2	2348.7	86576.2
Combination 3		**Combination 4**	
BMD equation	E-BMD equation	BMD equation	E-BMD equation
$\rho=1.122*HU+47$	$E=2.20*\rho-209$	$\rho=1.122*HU+4$	$E=0.1127\rho^{1.746}$
ρ (mg HA/cm^3)	Elastic modulus (MPa)	ρ (mg HA/cm^3)	Elastic modulus (MPa)
960.5	1904.0	960.5	18169.4
1151.8	2324.9	1151.8	24950.3
1343.1	2745.8	1343.1	32628.5
1534.4	3166.7	1534.4	41169.4
1725.7	3587.6	1725.7	50544.3
1917.0	4008.5	1917.0	60728.6
2108.3	4429.4	2108.3	71700.9
2299.7	4850.2	2299.7	83442.2
2491.0	5271.1	2491.0	95936.0
2682.3	5692.0	2682.3	109167.0

4.4.1. Correlation between mid-shaft peak stress and cortical wall thickness and mechanical parameters based on FE models with gray value-based material assignment

The correlations between peak stress of mid-shaft tibia and cortical wall thickness (p = 0.0536, R^2 = 0.041), bending stiffness (p = 0.787, R^2 = 0.001), maximal load (p = 0.772, R^2 = 0.001), work to fracture (p = 0.601, R^2 = 0.003), and maximal displacement (p = 0.569, R^2 = 0.004) were not significant, as shown in Figure 30.

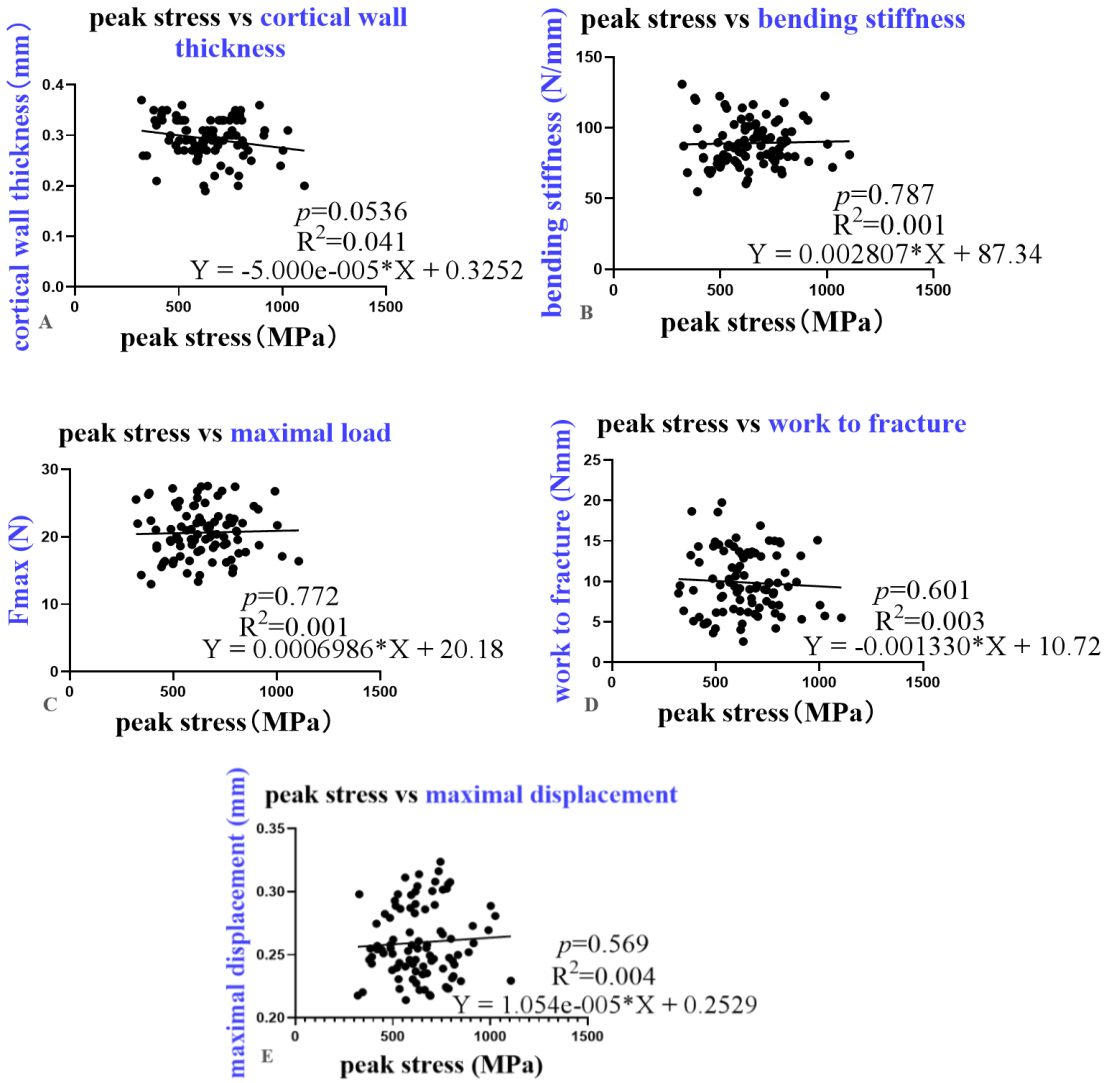

Figure 30. Correlation between peak stress and bending stiffness as well as cortical thickness. (A) Pearson correlation between peak stress and mid-shaft cortical wall thickness (p = 0.0536, R^2 = 0.041). (B) Pearson correlation between peak stress and bending stiffness (p = 0.787, R^2 = 0.001). (C) Pearson correlation between peak stress and maximal load (p = 0.772, R^2 = 0.001) (D)

Pearson correlation between peak stress and work to fracture (p = 0.601, R^2 = 0.003). (E) Pearson correlation between peak stress and maximal displacement (p = 0.569, R^2 = 0.004). The sample size was 91.

4.4.2. Correlation between axial stiffness and mechanical parameters based on FE models with gray value-based material assignment

The correlations between axial stiffness and work to fracture (p = 0.852, R^2 = 0.000), post-yield displacement (p = 0.406, R^2 = 0.008), maximal displacement (p = 0.648, R^2 = 0.002), bending stiffness (p = 0.403, R^2 = 0.008), and maximal load (p = 0.309, R^2 = 0.012) were not significant, as shown in Figure 31.

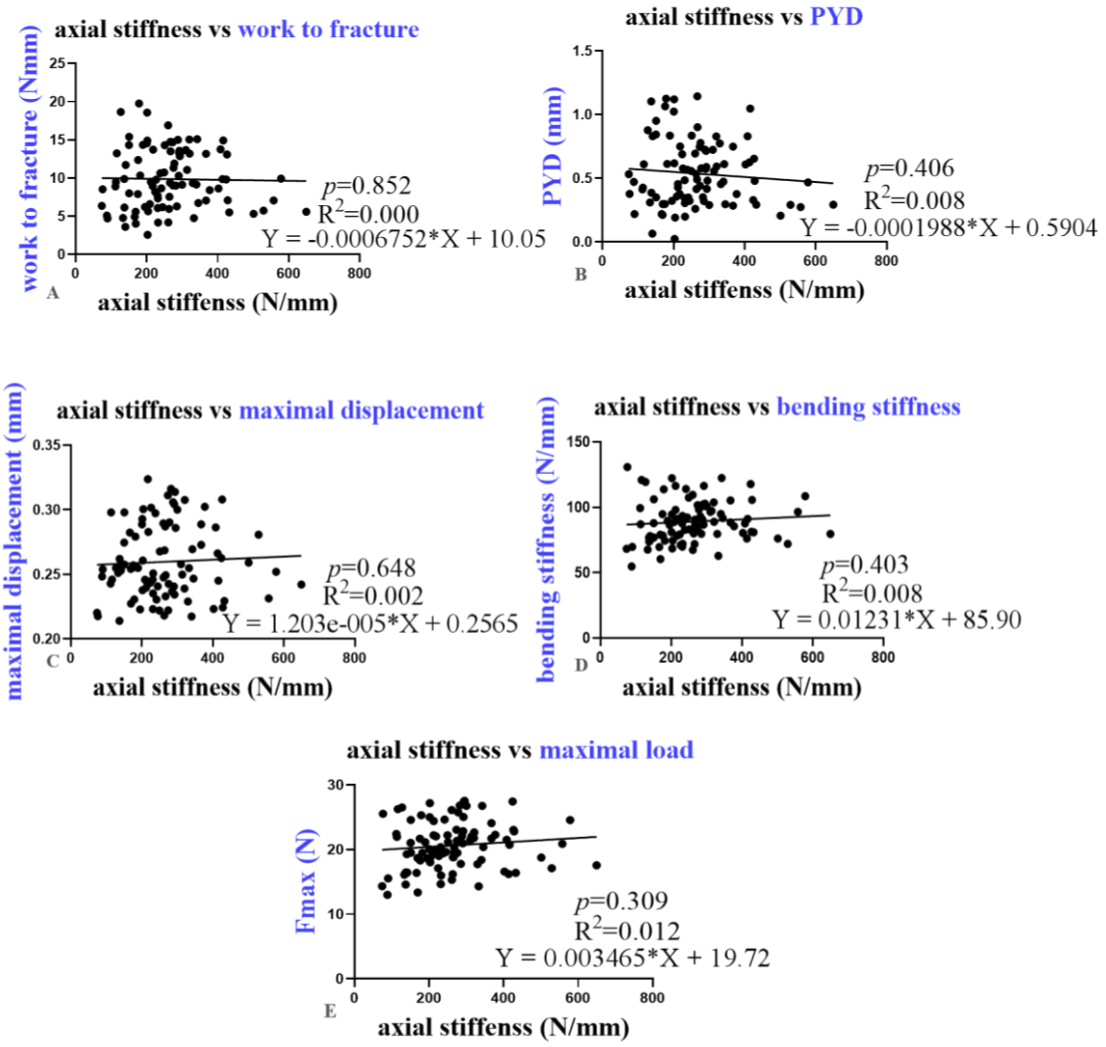

Figure 31. Correlation between axial stiffness and mechanical parameters. (A) Pearson correlation between axial stiffness and work to fracture (p = 0.852, R^2 = 0.000). (B) Pearson correlation between axial stiffness and post-yield displacement (p = 0.406, R^2 = 0.008). (C)

Pearson correlation between axial stiffness and maximal displacement (p = 0.648, R^2 = 0.002). (D) Pearson correlation between axial stiffness and bending stiffness (p = 0.403, R^2 = 0.008). (E) Pearson correlation between proximal stiffness and maximal load (p = 0.309, R^2 = 0.012). The sample size was 91.

4.4.3. Correlation between proximal stiffness and trabecular morphological parameters based on FE models with gray value-based material assignment

Pearson correlation analysis was conducted to study the correlation between proximal stiffness and the measured morphological parameters, namely BV/TV, Tb. Th, and Tb. Sp. Unfortunately, the correlations between proximal stiffness and BV/TV (p = 0.505, R^2 = 0.005), BS/BV (p = 0.857, R^2 = 0.000), Tb. Th. (p = 0.800, R^2 = 0.001), Tb. Sp. (p = 0.134, R^2 = 0.025), Tb. Pf. (p = 0.797, R^2 = 0.001), and Tb. N. (p = 0.283, R^2 = 0.013) were not significant, as shown in Figure 32.

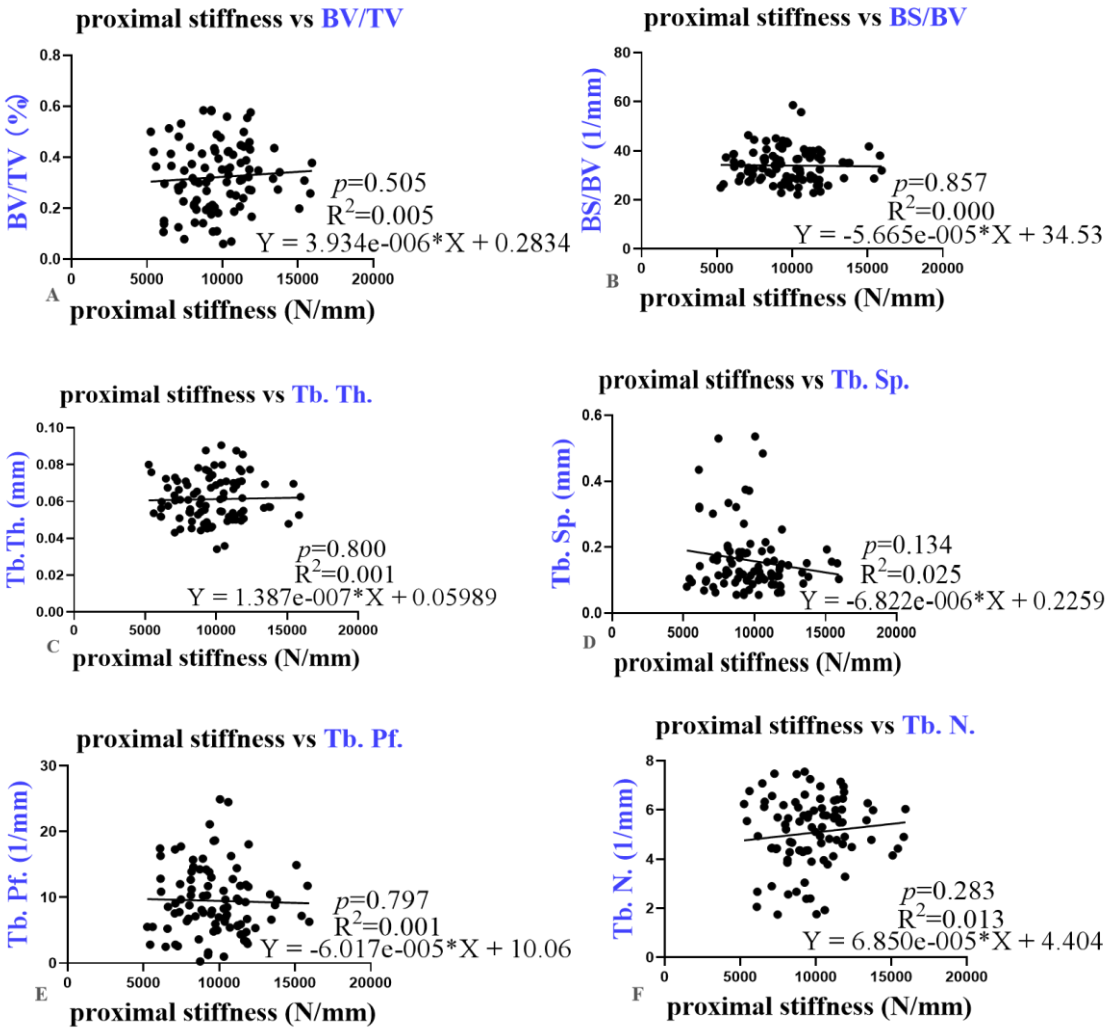

Figure 32. Correlation between proximal stiffness and trabecular morphological parameters. (A) Pearson correlation between proximal stiffness and BV/TV (p = 0.505, R^2 = 0.005). (B) Pearson correlation between proximal stiffness and BS/BV (p = 0.857, R^2 = 0.000). (C) Pearson correlation between proximal stiffness and Tb. Th. (p = 0.800, R^2 = 0.001). (D) Pearson correlation between proximal stiffness and Tb. Sp. (p = 0.134, R^2 = 0.025). (E) Pearson correlation between proximal stiffness and Tb. Pf. (p = 0.797, R^2 = 0.001). (F) Pearson correlation between proximal stiffness and Tb. N. (p = 0.283, R^2 = 0.013). The sample size was 91.

4.5. Establishment of three-point bending FEA based on the micro-CT data of WISP1 knockout mice

Due to the unsatisfactory correlation results of axial FE models with the experimentally measured parameters, the FEA strategy had to be reconsidered. One possible reason for the disappointing performance could be the different loading conditions between the biomechanical test, which was under a three-point bending setup, and the FE models, which were under axial loading conditions. To solve this problem, a new FE model simulating the three-point bending setup is needed, which could be validated by comparing the calculated bending stiffness with the experimentally measured bending stiffness. The general workflow is displayed in Figure 33.

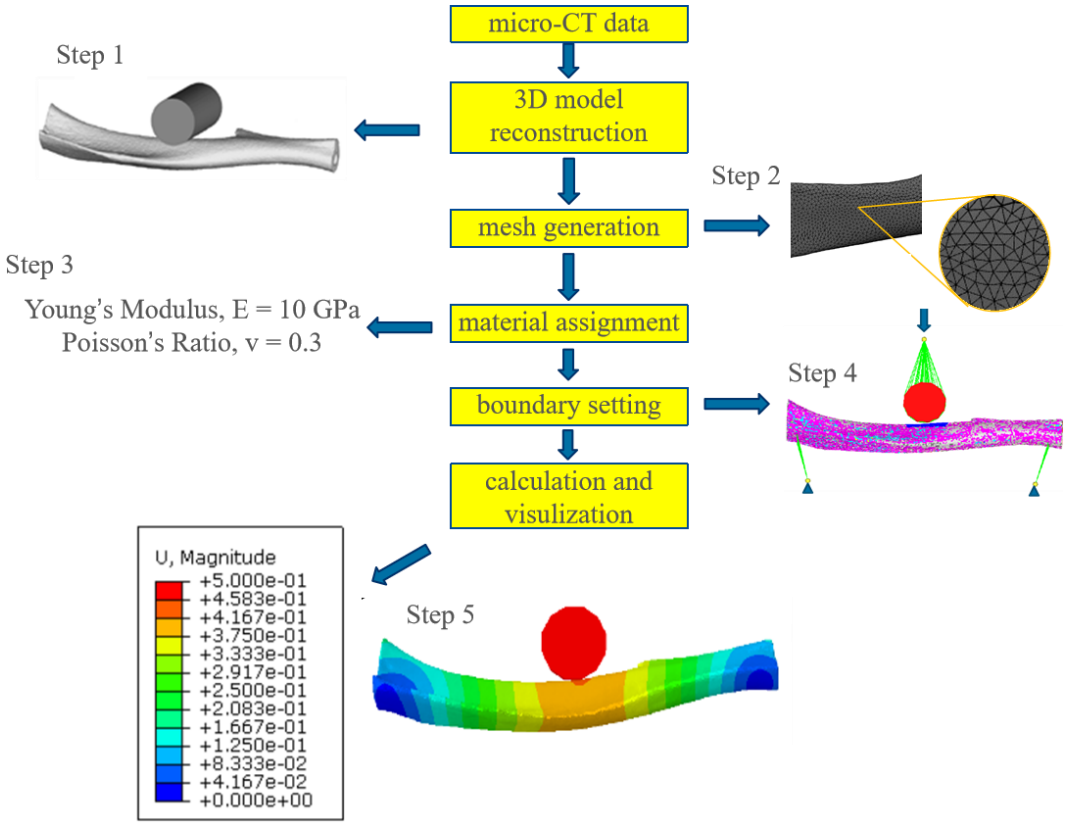

Figure 33. Workflow of creating an FE model to mimic the three-point bending setup. Step 1: construction of 3D geometric models based on micro-CT data. Step 2: mesh generation based on 3D geometric models. Step 3: material properties assigned into volume meshes. Step 4: setting loading and boundary conditions. Step 5: calculating the 3D models and visualizing results.

4.5.1. The sensitivity test for the mesh size of three-point bending FE models

Mesh size is believed to significantly impact the precision of FEA simulation (Liu et al., 2020). In the case of FEA simulating a three-point bending test, the nonlinearity of boundary conditions and the mesh size significantly impact computing costs. In the pre-experiment, the performance of the computer could not meet the experimental needs when the mesh size was set as 0.04 mm (the minimal pixel size of micro-CT scanning). Consequently, a mesh size sensitivity test was employed to determine the optimal mesh size that would achieve a good balance between accurate simulation and affordable computational costs. FE models with different mesh sizes ranging from 0.04 to 0.3 mm were compared in terms of bending stiffness. As bending stiffness calculated with a mesh size of 0.08 mm was quite close to that of a mesh size of 0.04 mm—with a deviation of only 4.16%—a mesh size of 0.08 mm was chosen as optimal for calculation, as shown in Figure 34. For models with a mesh size of 0.08 mm, the mean ± standard deviation number of elements and nodes was 116215 ± 2634 and 10942 ± 298, respectively.

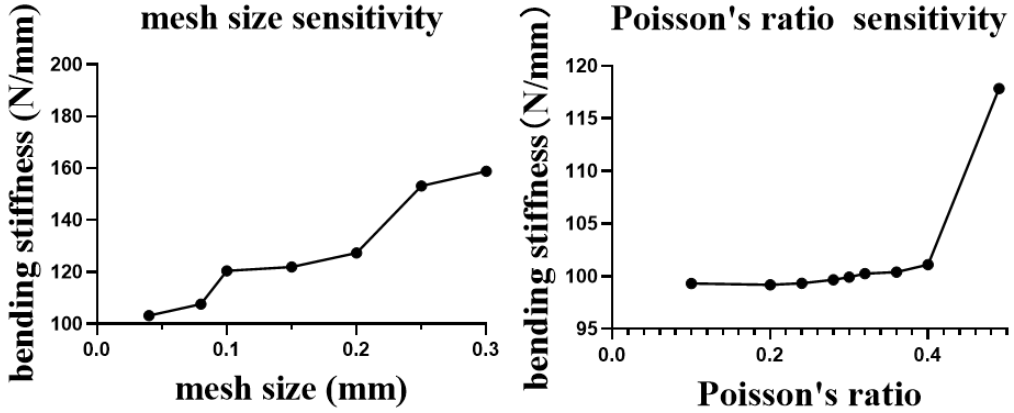

Figure 34. Mesh size sensitivity test (left) and Poisson's ratio sensitivity test (right). Bending stiffness increased as the mesh size increased. Bending stiffness calculated with a mesh size of 0.08 mm was quite close to that of a mesh size of 0.04 mm, with a deviation of only 4.16%. The calculated bending stiffness did not show significant variation, with Poisson's ratio ranging from 0.1 to 0.4. However, bending stiffness increased drastically when Poisson's ratio reached 0.5.

4.5.2. The sensitivity test for Poisson's ratio of three-point bending FE models

Poisson's ratio characterizes the Poisson effect in solid mechanics. It describes the deformation of a material in a direction perpendicular to a particular direction of loading (LourenCo *et al.*, 2020; Mokbel *et al.*, 2020; Terzi *et al.*, 2019). For most materials, Poisson's ratio is between 0.0 and 0.5. For soft materials in which the bulk modulus is much higher than the shear modulus, such as rubber, Poisson's ratio is close to 0.5 (Gross and Kress, 2017). For open-cell polymer foams, Poisson's ratio is close to 0 because cells tend to collapse when compressed (Duval *et al.*, 2013). In many typical solids, Poisson's ratio ranges from 0.2 to 0.3. Poisson's ratio sensitivity analysis was performed in this study, as shown in Figure 34. The difference in bending stiffness was minimal, with Poisson's ratio ranging from 0.1 to 0.4. As a result, Poisson's ratio of 0.3 (Heveran *et al.*, 2019) was used in the study.

4.5.3. Calculation of bending stiffness based on the three-point bending FE model with homogeneous material assignment

For homogeneous material assignment, Young's modulus was set as 10 Gpa and Poisson's ratio was set as 0.3. The three-point bending FE model was validated by comparing the calculated and experimentally measured bending stiffness. The calculated bending stiffness was 48.85 ± 6.67 N/mm, while the experimentally measured bending stiffness was 116.9 ± 17.93 N/mm, a difference of 41.79% (p = 0.001). More specifically, as shown in Table 10, bending stiffness of knockout mice calculated by the FE model was 45.91 ± 5.361 N/mm, and bending stiffness measured experimentally was 113.4 ± 3.751 N/mm, a difference of 59.51% (p = 0.016). Similarly, for wild-type mice the calculated bending stiffness was 51.42 ± 6.932 N/mm, and the experimentally measured bending stiffness was 119.9 ± 24.66 N/mm, a difference of 57.11% (p = 0.008). The results showed that the FE model significantly underestimated bending stiffness.

Table 10. Comparison of knockout and wild-type mice in terms of bending stiffness calculated by the FE model with the homogeneous material assignment and measured experimentally.

	Model		
	Stiffness (sim) (N/mm)	Stiffness (exp) (N/mm)	Difference/Significance
WISP knock-out (7)	45.91±5.361	113.4±3.751	59.51%/ *p*=0.016
WT (8)	51.42±6.932	119.9±24.66	57.11%/ *p*=0.008
Difference/Significance	10.72%/ *p*=0.189	5.42%/ *p*=0.47	
In total (15)	48.85±6.67	116.9±17.93	41.79%/ *p*=0.001

4.5.4. Validation of the three-point bending model by comparing bending stiffness calculated based on the FE model with the homogeneous material assignment that was measured experimentally

The linear regression model showed that bending stiffness calculated based on the FE model correlated positively and significantly with bending stiffness measured experimentally with a three-point bending test ($p < 0.001$, $R^2 = 0.5852$), as shown in Figure 35.

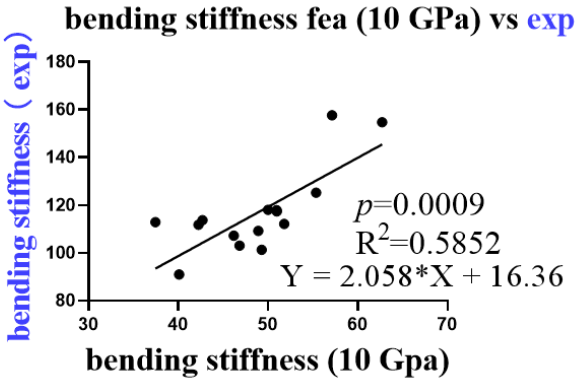

Figure 35. Correlation between bending stiffness calculated by the FE model and measured experimentally. Pearson correlation was conducted with $p < 0.001$ and $R^2 = 0.5852$. The sample size was 15.

4.6. Create an FE model to mimic a three-point bending setup with heterogeneous material assignment

Although the correlation analysis demonstrated a significant correlation, it seems that the homogeneous elastic modulus of 10 GPa was underestimated. Hence, a new method with heterogeneous material assignment was employed for better simulation. The relationship

between density and the HU value was calculated based on calibration of the micro-CT used, as mentioned in the methods section. The correlation between Young's modulus and the density was obtained from the literature (Currey, 1988; Kopperdahl *et al.*, 2002). To determine the optimal equation for further simulation, two equation combinations were compared in terms of the elastic modulus range, as shown in Table 11. For the first equation combination, the elastic modulus ranged from 540.3 to 37398.2 MPa, with a mean of 15370.5 MPa. For the second equation combination, the elastic modulus ranged from 742.9 to 10191.0 MPa, with a mean of 5465.2 MPa. Because the previous data showed that the elastic modulus of 10000 Mpa was underestimated, the first equation combination was chosen for the subsequent analysis.

Table 11. The equation combinations and material property gradient. Density was calculated based on the HU value. The elastic modulus was calculated using density. Based on the previously published literature, Poisson's ratio was set as 0.3 (Heveran *et al.*, 2019).

Combination1		**Combination2**	
BMD equation	**E-BMD equation**	**BMD equation**	**E-BMD equation**
ρ=0.206*HU-13.13	$E=0.1127\rho^{1.746}$	ρ=0.206*HU-13.13	E=7.136*ρ-172.3
ρ (mg HA/cm^3)	Elastic modulus (MPa)	ρ (mg HA/cm^3)	Elastic modulus (MPa)
128.3	540.3	128.3	743.0
275.4	2051.3	275.4	1792.8
422.5	4331.0	422.5	2824.5
569.6	7296.9	569.6	3892.3
716.7	10898.0	716.7	4942.1
863.8	15097.8	863.8	5991.9
1010.9	19868.4	1010.9	7041.7
1158.0	25187.3	1158.0	8091.4
1305.1	31035.8	1305.1	9141.2
1452.3	37398.2	1452.3	10191.0

4.6.1. Calculation of bending stiffness based on the three-point bending setup FE model with heterogeneous material assignment

Bending stiffness of the three-point bending setup was calculated as the loading force divided by the maximal displacement of the tibia. The experimentally measured bending stiffness was 116.2 ± 18.2 N/mm. Bending stiffness predicted by the FE model was 114.2

± 15.3 N/mm. There was no difference between the experimentally measured and calculated bending stiffness, with a deviation of only 1.72% (p = 0.47). More specifically, as shown in Table 13, bending stiffness of knockout mice calculated by the FE model was 111.5 ± 6.7 N/mm, and bending stiffness measured experimentally was 113.4 ± 3.8 N/mm, with a deviation of 1.68% (P=0.69). Similarly, for wild-type mice bending stiffness calculated by the FE model was 116.4 ± 20.4 N/mm, and bending stiffness measured experimentally was 119.9 ± 24.7 N/mm, with a deviation of 2.92% (p = 0.25).

Table 13. Comparison of knockout and wild-type mice in terms of bending stiffness calculated by the FE model with the heterogeneous material assignment and bending stiffness measured experimentally.

Gene type	Model		
	Stiffness (FE) (N/mm)	Stiffness (exp) (N/mm)	Difference/Significance
WISP knock-out (7)	111.5±6.7	113.4±3.8	1.68%/ p =0.69
WT (8)	116.4±20.4	119.9±24.7	2.92%/P=0.25
Difference/Significance	4.21%/ p =0.58	5.42%/ p =0.47	
In total (15)	114.2±15.3	116.9±18.0	1.72%/ p =0.47

4.6.2. Validation of the three-point bending model with heterogeneous material assignment

Pearson correlation analysis revealed that bending stiffness calculated with the FE model correlated positively with bending stiffness measured experimentally with a three-point bending test ($p < 0.001$, $R^2 = 0.9482$). The R^2 value close to 1 indicates a good correlation between the calculated and experimentally measured bending stiffness, as shown in Figure 36.

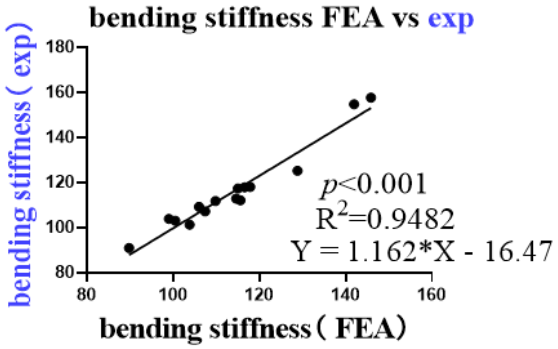

Figure 36. Correlation between bending stiffness calculated by FE model and measured experimentally. Pearson correlation was conducted with $p < 0.001$ and $R^2 = 0.9482$. The sample size was 15.

5. Discussion

5.1. Development of FEA and its application in bone mechanics

FEA is a numerical approach to provide approximate solutions to boundary value problems. In this approach, the problem region is disintegrated into simple parts (Lewis *et al.*, 2021; Naoum *et al.*, 2021; Schileo and Taddei, 2021). This method was first applied to calculate structural mechanics in industrial fields such as aircraft manufacturing and has been rapidly improved with the development of engineering, mathematics, and computer technology (Fadiji *et al.*, 2021; Vurtur Badarinath *et al.*, 2021). Its application has now been extended to the field of biomechanics of living organisms (Lewis *et al.*, 2021; Naoum *et al.*, 2021).

With the leap in computer technology, the resolution of FE models has also evolved from macro and rough data models to accurate microscale data models (Bevill and Keaveny, 2009). μFEA, based on a large amount of data from microscale image scanning and immense computing power, has shown broad application prospects in the reconstruction and simulation of the microstructure of human bone tissue (Herblum *et al.*, 2013; Lin *et al.*, 2014). Recently, there have been reports of good results from the combined application of μFEA, CAD, and rapid prototyping (RSP) techniques to assist in the fabrication of biomimetic bone tissue engineering scaffolds (Jaecques *et al.*, 2004). As

FE technology continues to evolve to evaluate microstructures and the constant expansion of microscale computing and simulation capabilities, the establishment and application of high-quality, large-scale data models have demonstrated outstanding potential in the study of bone mechanics (Karasik *et al.*, 2017; Ovesy *et al.*, 2019).

5.2. The aim of this study

In the present study, the FE technique was explored as an alternative approach to characterize biomechanical parameters and to reduce the number of mice required for experiments. Two types of FE models with axial loading and one FE model simulating a three-point bending setup were created. Besides, homogeneous and gray value-based heterogeneous material assignments were compared. Different FE models were created and then validated to determine the optimal FE model to characterize the biomechanical properties of mouse tibiae. The validation involved comparing FE-calculated parameters with experimentally measured morphological and mechanical parameters.

5.3. FE models with axial loading based on micro-CT data from TLR knockout mouse tibia

Two types of FE models were created with axial loading to characterize the mechanical properties of the whole tibia and the proximal part of the tibia. The axial stiffness and peak stress can be calculated based on the whole tibia model with axial loading. The axial stiffness of the proximal tibia was computed using the proximal tibia model with axial loading, as shown in Figure 37.

Neither material assignment method produced significant correlations between FE-calculated proximal stiffness and morphological parameters of trabecular bone. This outcome can be explained by the selection of different regions of interest (ROIs) for morphological parameter measurements and FE model simulation. As shown in Figure 37 (A and B), the proximal bending stiffness predicted by FEA was for the entire part of the proximal tibia. However, for the experimentally measured morphological trabecular

parameters, the ROI was a fixed cube volume within the trabecular bone (marked with white blocks).

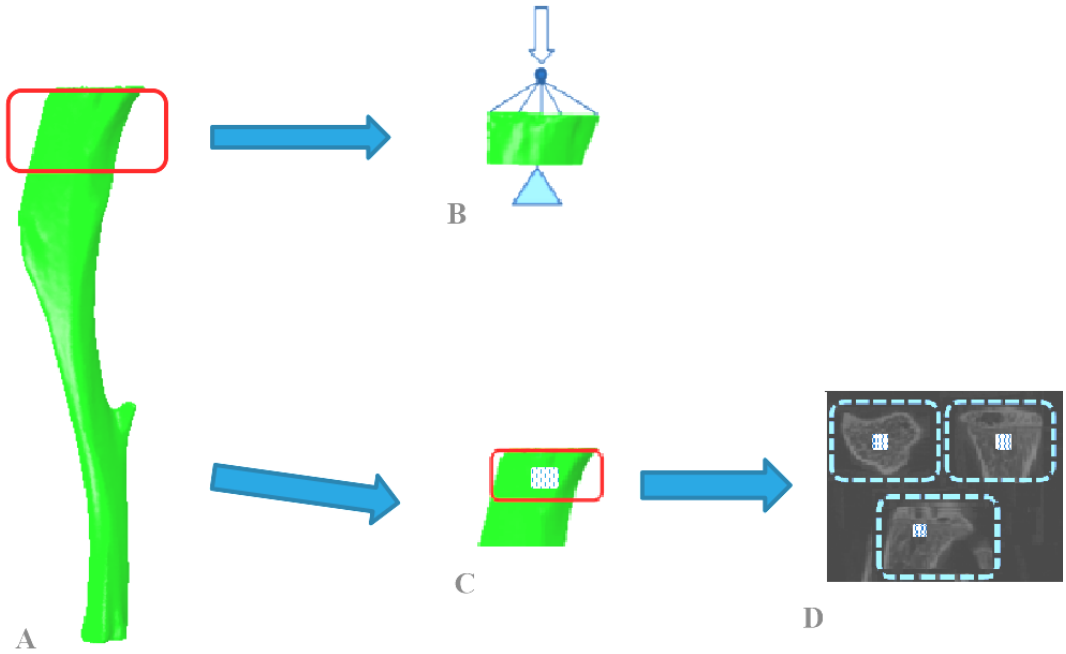

Figure 37. The ROIs for the axial loading FE model and morphological parameter measurement. The proximal part of the tibia was selected as ROI for the axial loading FE model, as plotted in A and B. A fixed cube volume (dimensions: 0.823 × 0.588 × 0.49 mm, 0.237 mm^3) was selected as the ROI to evaluate the bone parameters of the trabecula, as shown in C and D.

Similarly, neither material assignment method produced significant correlations between the calculated and experimentally measured mechanical parameters of trabecular bone. The non-significant correlations may be attributed to the difference in the loading pattern (Patel *et al.*, 2014). However, there was a negative correlation between peak stress and the mid-shaft cortical wall thickness (p = 0.014, R^2 = 0.068) with the homogeneous material assignment. This may be explained by the equation below:

$$Stress = \frac{loading\ \ force}{cros - sectional\ \ area}$$

A thinner cortical wall means that the cross-sectional area is smaller. With the same loading condition, stress increases when the cross-sectional area decreases (Carriero *et al.*, 2021).

5.4. FE models that can directly mimic the biomechanical testing procedure are needed

The correlation between parameters calculated based on FE models of axial loading and experimentally measured parameters was imperfect. The main reason could be that the parameters calculated based on FE models did not directly characterize the experimentally measured parameters (Oefner *et al.*, 2021). One typical experimental approach to characterize the biomechanical properties of the tibia is the bending test with a three-point bending setup (Collins *et al.*, 2021). FE models that can directly mimic the biomechanical testing setup should be created to better characterize the biomechanical properties of mouse tibia and can be more easily validated as the predicted parameters share similar loading modalities with that measured experimentally. Consequently, an FE model to simulate a three-point bending setup and to calculate bending stiffness was created.

5.5. FE models to simulate a three-point bending setup based on micro-CT data from WISP1 knockout mouse tibia demonstrated satisfactory correlation

The three-point bending FE model was validated by comparing the calculated and experimentally measured bending stiffness. So far, no validated three-point bending FE models based on mouse tibia have been reported. However, three-point bending FE models based on rat femurs have been reported. Arias-Moreno *et al.* (2020) used micro-CT-based FEA to predict bending stiffness of rat femur with a typical three-point bending setting. They reported an R^2 of 0.879 for bending stiffness. Besides, validated FE models with axial loading based on mouse tibia have been reported. Oliviero *et al.* (2021) compared different micro-CT-based FM models to predict the axial stiffness of mouse tibia under compressive load. The correlation between experimental and predicted stiffness was significant, with an R^2 ranging from 0.53 to 0.65. In the present study, for the FE model with heterogeneous material assignment, the linear regression model was significant ($p < 0.001$, $R^2 = 0.9482$), indicating good prediction of bending stiffness based

on the FE model with heterogeneous material assignment. Therefore, the FE model represents a potential alternative way to characterize the material behavior of mouse tibia in the linear elastic phase.

5.6. Comparison of FE methods with other computational simulation methods

Several computational methods have been used to characterize the biomechanical properties of bones. Among them, beam theory—a straightforward method—has been widely studied. The benefits of beam theory are enormous and stem from the significant reduction in time required for beam theory models (Pickering *et al.*, 2022). Indeed, the model usually takes seconds to simulate the tibial diaphysis. The fast nature of beam theory allows strain estimation immediately after micro-CT scans (Pereira *et al.*, 2015). Arias-Moreno *et al.* (2020) investigated how to predict bending stiffness of a rat femur in a typical three-point bending setting using beam theory; they demonstrated a good approximation of bending stiffness with an R^2 of 0.848. However, it should be noted that the precondition for the successful application of beam theory is the approximation of bone as a slender beam-like shape, which indicates that it may not be suitable for short or irregularly shaped bones such as vertebrae and the talus. Collins *et al.* (2021) compared the accuracy of beam theory and FEA to characterize bending stiffness based on a bone surrogate. FEA demonstrated better accuracy for the prediction, but beam theory overestimated bending stiffness. Similarly, Arias-Moreno *et al.* (2020) found that micro-CT-based FEA demonstrated better accuracy than beam theory in terms of bending stiffness prediction based on rat femur with a three-point bending setup. Given the limitation of the beam theory prediction, FE models were created and investigated in this study.

5.7. The choice of the tetrahedral element

For FEA of the mouse tibia, the meshing element type is mainly divided into four-node tetrahedral elements and eight-node regular hexahedral elements (Nazemi *et al.*, 2015). The advantage of the four-node tetrahedral mesh is that, in most cases, it can

automatically generate meshes for 3D models and has excellent geometric versatility and element size transition capabilities. In this thesis, the tetrahedral mesh, which can automatically generate meshes for the 3D model (Lewis *et al.*, 2021), was selected as the meshing method for the mouse tibia due to the aforementioned merits. However, the disadvantage is its linear interpolation function, resulting in greater stiffness. In addition, for the same geometry and element size, four-node tetrahedral partitioning requires more elements than eight-node hexahedral partitioning (Nazemi *et al.*, 2015). However, due to the improvement in computing power, these disadvantages can be offset by increasing the number of elements.

The eight-node hexahedral element has also been applied in many studies and has shown satisfactory simulation accuracy. Wang *et al.* (2015) used a hexahedral pixel mesh to determine the elastic modulus and yield strength of trabecular and found that for linear elastic problems, it still has quite high reliability. Prasad *et al.* (2010) established a mouse tibial cortical bone defect model using a hexahedral pixel grid with satisfactory simulation results. The advantage of the eight-node regular hexahedral element is that it avoids the possible geometric distortion of the tetrahedral element and thus has good robustness, but the disadvantage is that it often produces poor-quality elements near the boundary (Nazemi *et al.*, 2015). In addition, the meshing technique required for hexahedral element meshing is more demanding than tetrahedral elements, as it cannot be automatically generated for models with irregular shapes (Oliviero *et al.*, 2021). This is the crucial reason why it was not adopted in this study.

5.8. Material assignment

To simulate bone mechanics as accurately as possible, one of the biggest challenges is distributing material parameters to simulate bone material heterogeneity. It has been reported that heterogeneous material property distribution demonstrates superior simulation accuracy compared with homogeneous material distribution (Bourne and van der Meulen, 2004). One popular strategy for material property distribution is to consider

the micro-CT gray value distribution as the index to characterize material heterogeneity (Liu *et al.*, 2020). In this study, heterogeneous material property assignment was achieved by converting the gray value (represented as the HU value in Mimics software) to the bone density and, subsequently, the elastic modulus. Gray value-based material assignment showed superiority over homogeneous material assignment in three-point bending models (Xin *et al.*, 2013).

Elastic moduli are typically defined by imaging BMD and E-BMD equations derived from isolated compression tests of excised bone samples (Helgason *et al.*, 2008). As shown by Schileo *et al.* (2007), selection of the E-BMD equation is a critical factor in controlling the accuracy of the FE model. They compared three E-BMD equations from the literature and found that the accuracy of prediction varied greatly, with R^2 ranging from 0.554 to 0.911. In this study, the combination of E-BMD and BMD equations reported in the literature (Currey, 1988; Kopperdahl *et al.*, 2002; Perren, 1975) was carefully selected to ensure optimal elastic modulus prediction and was used for heterogeneous material assignment.

5.9. Limitations

Some limitations are inherent in establishing the FE model with a three-point bending setup or axial loading. First, the models created in the present study are a simplification of realistic settings. The three-point bending FE model can only mimic the elastic phase of the entire load-displacement curve, as shown in Figure 38. The yield strength or the fracture pattern cannot be simulated based on the models. Second, for the gray value-based material assignment, the correlation equations of density and elastic modulus were obtained from the literature instead of from direct measurement. The relationship between density and the HU value was also obtained from the literature for FE models with axial loading. Consequently, the accuracy of the simulation may be compromised. Third, because bending stiffness can be measured experimentally in a non-destructive manner, FE models with *ex vivo* micro-CT do not show too much potential for reducing the

number of mice needed. Thus, more efforts are required to develop more meticulous FE models with three-point bending that can mimic the yield process and the fracture pattern based on *in vivo* or *ex vivo* micro-CT.

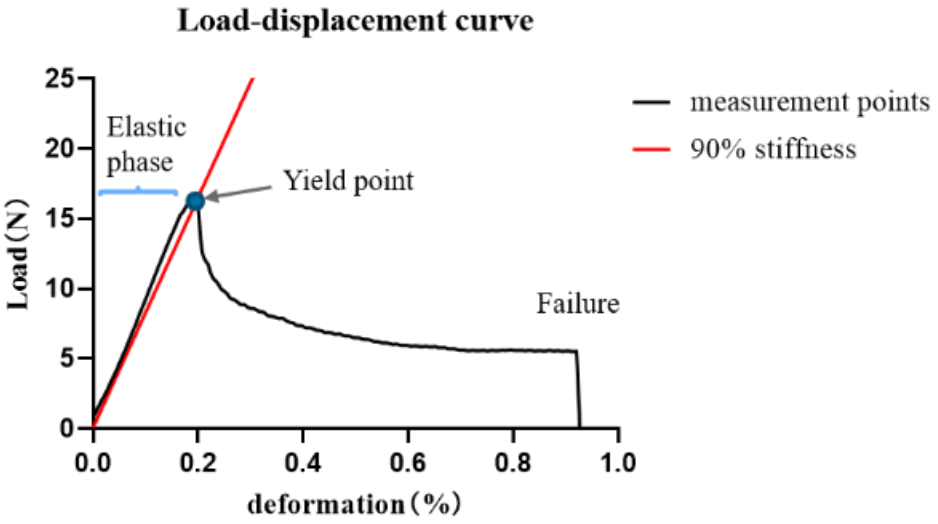

Figure 38. The load-displacement curve of mouse tibia experimentally loaded with a three-point- bending setup. It should be noted that the FE model can only mimic the elastic phase. The yield point was defined as the intersection between 90% stiffness and the load-displacement curve. The load decreased drastically after the failure point.

5.10. Outlook: FEA combined with *in vivo* micro-CT data may substantially reduce the number of mice used and allow monitoring bone adaptation over time

Currently, *in vivo* micro-CT scanning is gaining popularity to characterize bone morphological changes noninvasively (Arias-Moreno *et al.*, 2020), as it can measure the same animals at different time points. For example, protocols used to study osteoporosis or to analyze bone mass changes typically consider micro-CT scans to characterize cortical and cancellous morphological features (Zioupos *et al.*, 2008). Young *et al.* (2022) developed a novel method to detect and quantify site-specific differences in bone remodeling of 12-week-old BALB/c nude mice, which can characterize bone surface remodeling in mice across different anatomical regions. The method demonstrated great potential to detect early pathological events and it can track spatiotemporal development in both cortical and trabecular bone. In this case, *in vivo* micro-CT scans could reduce the number of mice required compared with *ex vivo* micro-CT scans because animals do not

need to be sacrificed at each experimental time point.

Besides, FE modeling based on *in vivo* micro-CT scan data can monitor the mechanical characteristics of the same animal at different time points. Oliviero *et al.* (2021) compared different FEA models with hexahedral or tetrahedral mesh and homogeneous or heterogeneous material properties generated from *in vivo* micro-CT images by comparing experimental stiffness with predicted stiffness. They found that hexahedral models with homogeneous material properties based on *in vivo* micro-CT images could best simulate the mechanical properties of the mouse tibia under axial loading. In this way, FEA could contribute to reduce the total number of experimental animals required by a study protocol, which fits the 3R principle well.

5.11. Conclusion

In conclusion, the FE model simulating three-point bending with heterogeneous material assignment based on micro-CT data of mouse tibiae showed good accuracy to stimulate linear elastic behavior of mouse tibia under a three-point bending setup. Besides, this FE model, in combination with *in vivo* micro-CT scanning, demonstrates great potential as an alternative *in silico* approach to reduce the number of animals needed for experiments and to save experimental time as well as costs.

6. Summary

FEA, based on a large amount of data from microscale image scanning and immense computing power, has shown great potential to simulate bone mechanics. This research intended to establish and validate FE models based on micro-CT data of mouse tibia to characterize the biomechanical properties.

The general steps for establishing an FE model include importing micro-CT data into Mimics software to create a 3D geometric model; creating 2D and 3D meshes based on a geometric model using 3-Matic software and Hypermesh software, respectively; assigning material properties using Mimics software; applying boundary conditions using Hypermesh software; and performing final computation as well as outcome parameter visualization using Abaqus software.

Two types of FE models of axial loading (whole tibia model and proximal tibia model) were established and validated by correlating the calculated and experimentally measured morphological and experimental parameters. However, the correlations were not significant. Later, bending stiffness was calculated and validated for the FE models simulating a three-point bending setup. The calculated and experimentally measured bending stiffness correlated positively for homogeneous ($p < 0.001$, $R^2 = 0.5852$) and heterogeneous ($p < 0.001$, $R^2 = 0.9482$) material assignment. However, the FE model with homogeneous material assignment significantly underestimated bending stiffness.

In conclusion, the FE model simulating three-point bending with heterogeneous material assignment based on micro-CT data of mouse tibiae showed good accuracy to simulate linear elastic behavior of mouse tibia under a three-point bending setup. Besides, this FE model, in combination with *in vivo* micro-CT scanning, demonstrates great potential as an alternative *in silico* approach to reduce the number of animals needed for experiments and to save experimental time as well as costs.

7. Zusammenfassung

Die FEA, die auf einer großen Menge von Daten aus mikroskaligen Bildaufnahmen und einer immensen Rechenleistung basiert, hat ein großes Potenzial für die Simulation der Knochenmechanik gezeigt. Ziel dieser Forschung war die Erstellung und Validierung von FE-Modellen auf der Grundlage von Mikro-CT-Daten der Tibia von Mäusen, um die biomechanischen Eigenschaften zu charakterisieren.

Die allgemeinen Schritte zur Erstellung eines FE-Modells umfassen den Import von Mikro-CT-Daten in die Mimics-Software zur Erstellung eines geometrischen 3D-Modells, die Erstellung von 2D- und 3D-Netzen auf der Grundlage eines geometrischen Modells mit der 3-Matic-Software bzw. der Hypermesh-Software, die Zuweisung von Materialeigenschaften mit der Mimics-Software, die Anwendung von Randbedingungen mit der Hypermesh-Software und die Durchführung der endgültigen Berechnung sowie die Visualisierung der Ergebnisparameter mit der Abaqus-Software.

Es wurden zwei Arten von FE-Modellen für axiale Belastung (Modell der gesamten Tibia und Modell der proximalen Tibia) erstellt und durch Korrelation der berechneten und experimentell gemessenen morphologischen und experimentellen Parameter validiert. Die Korrelationen waren jedoch nicht signifikant. Später wurde die Biegesteifigkeit für die FE-Modelle berechnet und validiert, wobei ein Dreipunkt-Biegeaufbau simuliert wurde. Die berechnete und experimentell gemessene Biegesteifigkeit korrelierte positiv für homogene ($p < 0,001$, $R2 = 0,5852$) und heterogene ($p < 0,001$, $R2 = 0,9482$) Materialzuordnung. Allerdings unterschätzte das FE-Modell mit homogener Materialzuordnung die Biegesteifigkeit deutlich.

Zusammenfassend lässt sich sagen, dass das FE-Modell, das die Dreipunkt-Biegung mit heterogener Materialzuweisung auf der Grundlage von Mikro-CT-Daten von Mäuseschienbeinen simuliert, eine gute Genauigkeit bei der Simulation des linearen

elastischen Verhaltens von Mäuseschienbeinen unter einer Dreipunkt-Biegung aufweist. Außerdem zeigt dieses FE-Modell in Kombination mit In-vivo-Mikro-CT-Scans ein großes Potenzial als alternativer In-silico-Ansatz, um die Anzahl der für Experimente benötigten Tiere zu reduzieren und sowohl Versuchszeit als auch Kosten zu sparen.

8. Bibliography

AFANASSIEVA, O. B. 2021. On the Planar Geometric Patterns of the Exoskeletal Relief Formation in Early Vertebrates (Osteostraci, Agnatha). *Dokl Biol Sci,* 496**,** 9-12.

ARIAS-MORENO, A. J., ITO, K. & VAN RIETBERGEN, B. 2020. Accuracy of beam theory for estimating bone tissue modulus and yield stress from 3-point bending tests on rat femora. *J Biomech,* 101**,** 109654.

ATAKE, O. J. & EAMES, B. F. 2021. Mineralized Cartilage and Bone-Like Tissues in Chondrichthyans Offer Potential Insights Into the Evolution and Development of Mineralized Tissues in the Vertebrate Endoskeleton. *Front Genet,* 12**,** 762042.

BARBE, M. F., AMIN, M., HARRIS, M. Y., PANIBATLA, S. T., ASSARI, S., POPOFF, S. N. & BOVE, G. M. 2022. Manual Therapy Facilitates Homeostatic Adaptation to Bone Microstructural Declines Induced by a Rat Model of Repetitive Forceful Task. *Int J Mol Sci,* 23.

BARBIER, A., MARTEL, C., DE VERNEJOUL, M. C., TIRODE, F., NYS, M., MOCAER, G., MORIEUX, C., MURAKAMI, H. & LACHERETZ, F. 1999. The visualization and evaluation of bone architecture in the rat using three-dimensional X-ray microcomputed tomography. *J Bone Miner Metab,* 17**,** 37-44.

BEHFOROOTAN, S., CHATZISTERGOS, P., NAEMI, R. & CHOCKALINGAM, N. 2017. Finite element modelling of the foot for clinical application: A systematic review. *Med Eng Phys,* 39**,** 1-11.

BELYTSCHKO, T., KULAK, R. F., SCHULTZ, A. B. & GALANTE, J. O. 1974. Finite element stress analysis of an intervertebral disc. *J Biomech,* 7**,** 277-85.

BEVILL, G. & KEAVENY, T. M. 2009. Trabecular bone strength predictions using finite element analysis of micro-scale images at limited spatial resolution. *Bone,* 44**,** 579-84.

BOURNE, B. C. & VAN DER MEULEN, M. C. 2004. Finite element models predict cancellous apparent modulus when tissue modulus is scaled from specimen CT-attenuation. *J Biomech,* 37**,** 613-21.

BREKELMANS, W. A., POORT, H. W. & SLOOFF, T. J. 1972. A new method to analyse the mechanical behaviour of skeletal parts. *Acta Orthop Scand,* 43**,** 301-17.

BRODT, M. D., ELLIS, C. B. & SILVA, M. J. 1999. Growing C57Bl/6 mice increase whole bone mechanical properties by increasing geometric and material properties. *J Bone Miner Res,* 14**,** 2159-66.

BURR, D. B., MILGROM, C., FYHRIE, D., FORWOOD, M., NYSKA, M., FINESTONE, A., HOSHAW, S., SAIAG, E. & SIMKIN, A. 1996. In vivo measurement of human tibial strains during vigorous activity. *Bone,* 18**,** 405-10.

CARBONE, L. & AUSTIN, J. 2016. Pain and Laboratory Animals: Publication Practices for Better Data Reproducibility and Better Animal Welfare. *PLoS One,* 11**,** e0155001.

CARRIERO, A., JAVAHERI, B., BASSIR KAZERUNI, N., PITSILLIDES, A. A. & SHEFELBINE, S. J. 2021. Age and Sex Differences in Load-Induced Tibial

Cortical Bone Surface Strain Maps. *JBMR Plus,* 5**,** e10467.
CASTILLO-MENDEZ, C. & ORTIZ, A. 2022. Numerical simulation data and FORTRAN code to compare the stress response of two transversely isotropic hyperelastic models in ABAQUS. *Data Brief,* 41**,** 107853.
CHAPPARD, D., BASLE, M. F., LEGRAND, E. & AUDRAN, M. 2008. Trabecular bone microarchitecture: a review. *Morphologie,* 92**,** 162-70.
CHEN, S. H., HSIAO, C. K., WANG, C. W., CHEN, H. H. & ZHONG, Z. C. 2022. Biomechanical Comparison between Isobar and Dynamic-Transitional Optima (DTO) Hybrid Lumbar Fixators: A Lumbosacral Finite Element and Intersegmental Motion Analysis. *Biomed Res Int,* 2022**,** 8273853.
CHEONG, V. S., ROBERTS, B. C., KADIRKAMANATHAN, V. & DALL'ARA, E. 2021. Positive interactions of mechanical loading and PTH treatments on spatio-temporal bone remodelling. *Acta Biomater,* 136**,** 291-305.
COLE, J. H. & VAN DER MEULEN, M. C. 2011. Whole bone mechanics and bone quality. *Clin Orthop Relat Res,* 469**,** 2139-49.
COLLINS, C. J., YANG, B., CRENSHAW, T. D. & PLOEG, H. L. 2021. Evaluation of experimental, analytical, and computational methods to determine long-bone bending stiffness. *J Mech Behav Biomed Mater,* 115**,** 104253.
COMPSTON, J. E. & CROUCHER, P. I. 1991. Histomorphometric assessment of trabecular bone remodelling in osteoporosis. *Bone Miner,* 14**,** 91-102.
CULMANN, K. 1866. *Die Graphische Statik.,* Zurich: Verlag von Meyer & Zeller.
CURREY, J. D. 1988. The effect of porosity and mineral content on the Young's modulus of elasticity of compact bone. *J Biomech,* 21**,** 131-9.
DE VOS, W., CASSELMAN, J. & SWENNEN, G. R. 2009. Cone-beam computerized tomography (CBCT) imaging of the oral and maxillofacial region: a systematic review of the literature. *Int J Oral Maxillofac Surg,* 38**,** 609-25.
DIAZ, L., ZAMBRANO, E., FLORES, M. E., CONTRERAS, M., CRISPIN, J. C., ALEMAN, G., BRAVO, C., ARMENTA, A., VALDES, V. J., TOVAR, A., GAMBA, G., BARRIOS-PAYAN, J. & BOBADILLA, N. A. 2020. Ethical Considerations in Animal Research: The Principle of 3R's. *Rev Invest Clin,* 73**,** 199-209.
DING, Z., WEI, W., WANG, K. & LIU, Y. 2022. An Ultrasonic Motor Using a Carbon-Fiber-Reinforced/Poly-Phenylene-Sulfide-Based Vibrator with Bending/Longitudinal Modes. *Micromachines (Basel),* 13.
DONAHUE, T. L., HULL, M. L., RASHID, M. M. & JACOBS, C. R. 2002. A finite element model of the human knee joint for the study of tibio-femoral contact. *J Biomech Eng,* 124**,** 273-80.
DUVAL, E., DESCHAMPS, T. & SAVIOT, L. 2013. Poisson ratio and excess low-frequency vibrational states in glasses. *J Chem Phys,* 139**,** 064506.
FADIJI, T., ASHTIANI, S. M., ONWUDE, D. I., LI, Z. & OPARA, U. L. 2021. Finite Element Method for Freezing and Thawing Industrial Food Processes. *Foods,* 10.
FENG, X. & MCDONALD, J. M. 2011. Disorders of bone remodeling. *Annu Rev Pathol,* 6**,** 121-45.

FEYZI, M., FALLAHNEZHAD, K., TAYLOR, M. & HASHEMI, R. 2021. A review on the finite element simulation of fretting wear and corrosion in the taper junction of hip replacement implants. *Comput Biol Med,* 130**,** 104196.

FOLETTI, J. M., MARTINEZ, V., HAEN, P., GODIO-RABOUTET, Y., GUYOT, L. & THOLLON, L. 2019. Finite element analysis of the human orbit. Behavior of titanium mesh for orbital floor reconstruction in case of trauma recurrence. *J Stomatol Oral Maxillofac Surg,* 120**,** 91-94.

FRITTON, S. P., MCLEOD, K. J. & RUBIN, C. T. 2000. Quantifying the strain history of bone: spatial uniformity and self-similarity of low-magnitude strains. *J Biomech,* 33**,** 317-25.

FROST, H. M. 2001. From Wolff's law to the Utah paradigm: insights about bone physiology and its clinical applications. *Anat Rec,* 262**,** 398-419.

FROST, H. M. 2004. A 2003 update of bone physiology and Wolff's Law for clinicians. *Angle Orthod,* 74**,** 3-15.

GEFEN, A. & SELIKTAR, R. 2004. Comparison of the trabecular architecture and the isostatic stress flow in the human calcaneus. *Med Eng Phys,* 26**,** 119-29.

GHAVAMI-LAHIJI, M., DAVALLOO, R. T., TAJZIEHCHI, G. & SHAMS, P. 2021. Micro-computed tomography in preventive and restorative dental research: A review. *Imaging Sci Dent,* 51**,** 341-350.

GNEITING, E. 2017. *Bone Integrity in Toll-like Receptor Knockout Mice with Type 2 Diabetes Mellitus.* B.Sc. Medizintechnik, Eberhard-Karls University Tübingen.

GOYAL, A. & PRASAD, J. 2022. An in silico model for woven bone adaptation to heavy loading conditions in murine tibia. *Biomech Model Mechanobiol*.

GRASSI, L. & ISAKSSON, H. 2015. Extracting accurate strain measurements in bone mechanics: A critical review of current methods. *J Mech Behav Biomed Mater,* 50**,** 43-54.

GREEN, S. B. 2015. Can animal data translate to innovations necessary for a new era of patient-centred and individualised healthcare? Bias in preclinical animal research. *BMC Med Ethics,* 16**,** 53.

GROSS, W. & KRESS, H. 2017. Simultaneous measurement of the Young's modulus and the Poisson ratio of thin elastic layers. *Soft Matter,* 13**,** 1048-1055.

GUHA, I., ZHANG, X., RAJAPAKSE, C. S., CHANG, G. & SAHA, P. K. 2022. Finite element analysis of trabecular bone microstructure using CT imaging and continuum mechanical modeling. *Med Phys,* 49**,** 3886-3899.

HADJIDAKIS, D. J. & ANDROULAKIS, II 2006. Bone remodeling. *Ann N Y Acad Sci,* 1092**,** 385-96.

HARRIGAN, T. P., KAREH, J. A., O'CONNOR, D. O., BURKE, D. W. & HARRIS, W. H. 1992. A finite element study of the initiation of failure of fixation in cemented femoral total hip components. *J Orthop Res,* 10**,** 134-44.

HARTUNG, T. 2013. Look back in anger - what clinical studies tell us about preclinical work. *ALTEX,* 30**,** 275-91.

HELGASON, B., PERILLI, E., SCHILEO, E., TADDEI, F., BRYNJOLFSSON, S. & VICECONTI, M. 2008. Mathematical relationships between bone density and

mechanical properties: a literature review. *Clin Biomech (Bristol, Avon),* 23**,** 135-46.

HERBLUM, R., BEEK, M. & WHYNE, C. M. 2013. muFEA successfully exhibits higher stresses and strains in microdamaged regions of whole vertebrae. *J Orthop Res,* 31**,** 1653-60.

HEVERAN, C. M., SCHURMAN, C. A., ACEVEDO, C., LIVINGSTON, E. W., HOWE, D., SCHAIBLE, E. G., HUNT, H. B., RAUFF, A., DONNELLY, E., CARPENTER, R. D., LEVI, M., LAU, A. G., BATEMAN, T. A., ALLISTON, T., KING, K. B. & FERGUSON, V. L. 2019. Chronic kidney disease and aging differentially diminish bone material and microarchitecture in C57Bl/6 mice. *Bone,* 127**,** 91-103.

HOSHINO, K., TAKEUCHI, O., KAWAI, T., SANJO, H., OGAWA, T., TAKEDA, Y., TAKEDA, K. & AKIRA, S. 1999. Cutting edge: Toll-like receptor 4 (TLR4)-deficient mice are hyporesponsive to lipopolysaccharide: evidence for TLR4 as the Lps gene product. *J Immunol,* 162**,** 3749-52.

HUANG, X., NUSSLER, A. K., REUMANN, M. K., AUGAT, P., MENGER, M. M., GHALLAB, A., HENGSTLER, J. G., HISTING, T. & EHNERT, S. 2022. Contribution to the 3R Principle: Description of a Specimen-Specific Finite Element Model Simulating 3-Point-Bending Tests in Mouse Tibiae. *Bioengineering (Basel),* 9.

HUSS, M. K., FELT, S. A. & PACHARINSAK, C. 2019. Influence of Pain and Analgesia on Orthopedic and Wound-healing Models in Rats and Mice. *Comp Med,* 69**,** 535-545.

JAECQUES, S. V., VAN OOSTERWYCK, H., MURARU, L., VAN CLEYNENBREUGEL, T., DE SMET, E., WEVERS, M., NAERT, I. & VANDER SLOTEN, J. 2004. Individualised, micro CT-based finite element modelling as a tool for biomechanical analysis related to tissue engineering of bone. *Biomaterials,* 25**,** 1683-96.

JEPSEN, K. J., SILVA, M. J., VASHISHTH, D., GUO, X. E. & VAN DER MEULEN, M. C. 2015. Establishing biomechanical mechanisms in mouse models: practical guidelines for systematically evaluating phenotypic changes in the diaphyses of long bones. *J Bone Miner Res,* 30**,** 951-66.

KARASIK, D., DEMISSIE, S., LU, D., BROE, K. E., BOYD, S. K., LIU, C. T., HSU, Y. H., BOUXSEIN, M. L. & KIEL, D. P. 2017. Bone Strength Estimated by Micro-Finite Element Analysis (microFEA) Is Heritable and Shares Genetic Predisposition With Areal BMD: The Framingham Study. *J Bone Miner Res,* 32**,** 2151-2156.

KAU, A. L., AHERN, P. P., GRIFFIN, N. W., GOODMAN, A. L. & GORDON, J. I. 2011. Human nutrition, the gut microbiome and the immune system. *Nature,* 474**,** 327-36.

KHALAF, A. T., WEI, Y., WAN, J., ZHU, J., PENG, Y., ABDUL KADIR, S. Y., ZAINOL, J., OGLAH, Z., CHENG, L. & SHI, Z. 2022. Bone Tissue Engineering through 3D Bioprinting of Bioceramic Scaffolds: A Review and Update. *Life*

(Basel), 12.

KINNEY, J. H., LANE, N. E. & HAUPT, D. L. 1995. In vivo, three-dimensional microscopy of trabecular bone. *J Bone Miner Res,* 10**,** 264-70.

KOCH, J. C. 1917. The Laws of Bone Architecture. *American Journal of Anatomy,* 21**,** 177–289.

KOHLER, R., TASTAD, C. A., STACY, A. J., SWALLOW, E. A., METZGER, C. E., ALLEN, M. R. & WALLACE, J. M. 2021. The Effect of Single Versus Group muCT on the Detection of Trabecular and Cortical Disease Phenotypes in Mouse Bones. *JBMR Plus,* 5**,** e10473.

KOPPERDAHL, D. L., MORGAN, E. F. & KEAVENY, T. M. 2002. Quantitative computed tomography estimates of the mechanical properties of human vertebral trabecular bone. *J Orthop Res,* 20**,** 801-5.

LEWIS, G. S., MISCHLER, D., WEE, H., REID, J. S. & VARGA, P. 2021. Finite Element Analysis of Fracture Fixation. *Curr Osteoporos Rep,* 19**,** 403-416.

LI, G., QIAN, H., GUO, S., WANG, D., SUN, C., DU, Y., CHENG, J. & JIANG, H. 2019. Assessment of aging characteristics of female condylar trabecular structure by cone-beam computed tomography. *Oral Radiol,* 35**,** 16-22.

LI, J., WANG, Y., WEI, Y., KONG, D., LIN, Y., WANG, D., CHENG, S., YIN, P. & WEI, M. 2022a. The effect of talus osteochondral defects of different area size on ankle joint stability: a finite element analysis. *BMC Musculoskelet Disord,* 23**,** 500.

LI, S., XU, B., LIU, Y., ZHANG, J., XU, G., SHAO, P., LI, X., HU, Y. & MA, X. 2022b. Biomechanical Evaluation of Spinal Column after Percutaneous Cement Discoplasty: A Finite Element Analysis. *Orthop Surg.*

LIN, L., OON, H. Y., LIN, W. & QIN, Y. X. 2014. Principal trabecular structural orientation predicted by quantitative ultrasound is strongly correlated with muFEA determined anisotropic apparent stiffness. *Biomech Model Mechanobiol,* 13**,** 961-71.

LIU, B., ZHOU, Y., GU, L. & HUANG, X. 2020. Finite Element Simulation and Multi-Factor Stress Prediction Model for Cement Concrete Pavement Considering Void under Slab. *Materials (Basel),* 13.

LOUNDAGIN, L. L. & COOPER, D. M. L. 2022. Towards novel measurements of remodeling activity in cortical bone: implications for osteoporosis and related pharmaceutical treatments. *Eur Cell Mater,* 43**,** 202-227.

LOURENCO, A. L., JAGER, N., PROCHNOW, C., MILBRANDT DUTRA, D. A. & KLEVERLAAN, C. J. 2020. Young's modulus and Poisson ratio of composite materials: Influence of wet and dry storage. *Dent Mater J,* 39**,** 657-663.

LUO, C., JIANG, T., TIAN, S., YAO, J. & FAN, Y. 2022. Finite element analysis of shank and ankle with different boot collar heights in parachuting landing on inversion ground surface. *Comput Methods Biomech Biomed Engin,* 25**,** 953-960.

MACNEIL, J. A. & BOYD, S. K. 2008. Bone strength at the distal radius can be estimated from high-resolution peripheral quantitative computed tomography and the finite element method. *Bone,* 42**,** 1203-13.

MAIESE, K. 2022. Wnt Signaling and WISP1 (CCN4): Critical Components in Neurovascular Disease, Blood Brain Barrier Regulation, and Cerebral Hemorrhage. *Curr Neurovasc Res*.

MAKIDA, K., NISHIDA, Y., MORITA, D., OCHIAI, S., HIGUCHI, Y., SEKI, T., IKUTA, K. & ISHIGURO, N. 2020. Low energy irradiation of narrow-range UV-LED prevents osteosarcopenia associated with vitamin D deficiency in senescence-accelerated mouse prone 6. *Sci Rep,* 10**,** 11892.

MANCIOCCO, A., CHIAROTTI, F., VITALE, A., CALAMANDREI, G., LAVIOLA, G. & ALLEVA, E. 2009. The application of Russell and Burch 3R principle in rodent models of neurodegenerative disease: the case of Parkinson's disease. *Neurosci Biobehav Rev,* 33**,** 18-32.

MCNAMARA, B. P., CRISTOFOLINI, L., TONI, A. & TAYLOR, D. 1997. Relationship between bone-prosthesis bonding and load transfer in total hip reconstruction. *J Biomech,* 30**,** 621-30.

MERCAN, N., YILDIRIM, A. & DERE, Y. 2022. Biomechanical Analysis of Tibiofibular Syndesmosis Injury Fixation Methods: A Finite Element Analysis. *J Foot Ankle Surg*.

MILHEIRO, A., DE TOBEL, J., CAPITANEANU, C., SHAHEEN, E., FIEUWS, S. & THEVISSEN, P. 2022. Quantifying the potential of morphological parameters for human dental identification: part 1-proof of concept. *Int J Legal Med*.

MOKBEL, M., HOSSEINI, K., ALAND, S. & FISCHER-FRIEDRICH, E. 2020. The Poisson Ratio of the Cellular Actin Cortex Is Frequency Dependent. *Biophys J,* 118**,** 1968-1976.

MONTOYA, C., DU, Y., GIANFORCARO, A. L., ORREGO, S., YANG, M. & LELKES, P. I. 2021. On the road to smart biomaterials for bone research: definitions, concepts, advances, and outlook. *Bone Res,* 9**,** 12.

MULLER, R., VAN CAMPENHOUT, H., VAN DAMME, B., VAN DER PERRE, G., DEQUEKER, J., HILDEBRAND, T. & RUEGSEGGER, P. 1998. Morphometric analysis of human bone biopsies: a quantitative structural comparison of histological sections and micro-computed tomography. *Bone,* 23**,** 59-66.

NAOUM, S., VASILIADIS, A. V., KOUTSERIMPAS, C., MYLONAKIS, N., KOTSAPAS, M. & KATAKALOS, K. 2021. Finite Element Method for the Evaluation of the Human Spine: A Literature Overview. *J Funct Biomater,* 12.

NAZEMI, S. M., AMINI, M., KONTULAINEN, S. A., MILNER, J. S., HOLDSWORTH, D. W., MASRI, B. A., WILSON, D. R. & JOHNSTON, J. D. 2015. Prediction of local proximal tibial subchondral bone structural stiffness using subject-specific finite element modeling: Effect of selected density-modulus relationship. *Clin Biomech (Bristol, Avon),* 30**,** 703-12.

NELDAM, C. A. & PINHOLT, E. M. 2014. Synchrotron μCT imaging of bone, titanium implants and bone substitutes - a systematic review of the literature. *J Craniomaxillofac Surg,* 42**,** 801-5.

NEUHAUS, W. 2020. Consensus Statement from the European Network of 3R Centres (EU3Rnet). *ALTEX*.

NING, B., LONDONO, I., LAPORTE, C. & VILLEMURE, I. 2022. Validation of an in vivo micro-CT-based method to quantify longitudinal bone growth of pubertal rats. *Bone,* 154**,** 116207.

OEFNER, C., HERRMANN, S., KEBBACH, M., LANGE, H. E., KLUESS, D. & WOICZINSKI, M. 2021. Reporting checklist for verification and validation of finite element analysis in orthopedic and trauma biomechanics. *Med Eng Phys,* 92**,** 25-32.

OLIVIERO, S., ROBERTS, M., OWEN, R., REILLY, G. C., BELLANTUONO, I. & DALL'ARA, E. 2021. Non-invasive prediction of the mouse tibia mechanical properties from microCT images: comparison between different finite element models. *Biomech Model Mechanobiol,* 20**,** 941-955.

OVESY, M., INDERMAUR, M. & ZYSSET, P. K. 2019. Prediction of insertion torque and stiffness of a dental implant in bovine trabecular bone using explicit micro-finite element analysis. *J Mech Behav Biomed Mater,* 98**,** 301-310.

PARFITT, A. M. 1979. Quantum concept of bone remodeling and turnover: implications for the pathogenesis of osteoporosis. *Calcif Tissue Int,* 28**,** 1-5.

PATEL, T. K., BRODT, M. D. & SILVA, M. J. 2014. Experimental and finite element analysis of strains induced by axial tibial compression in young-adult and old female C57Bl/6 mice. *J Biomech,* 47**,** 451-7.

PAULUS, M. J., GLEASON, S. S., EASTERLY, M. E. & FOLTZ, C. J. 2001. A review of high-resolution X-ray computed tomography and other imaging modalities for small animal research. *Lab Anim (NY),* 30**,** 36-45.

PEREIRA, A. F., JAVAHERI, B., PITSILLIDES, A. A. & SHEFELBINE, S. J. 2015. Predicting cortical bone adaptation to axial loading in the mouse tibia. *J R Soc Interface,* 12**,** 0590.

PERREN, S. M. 1975. [Sutures and implants in surgery of the extremities]. *Chirurg,* 46**,** 447-53.

PICKERING, E., TRICHILO, S., DELISSER, P. & PIVONKA, P. 2022. Beam theory for rapid strain estimation in the mouse tibia compression model. *Biomech Model Mechanobiol,* 21**,** 513-525.

PISTOIA, W., VAN RIETBERGEN, B., LOCHMULLER, E. M., LILL, C. A., ECKSTEIN, F. & RUEGSEGGER, P. 2002. Estimation of distal radius failure load with micro-finite element analysis models based on three-dimensional peripheral quantitative computed tomography images. *Bone,* 30**,** 842-8.

PRADOS-PRIVADO, M., MARTINEZ-MARTINEZ, C., GEHRKE, S. A. & PRADOS-FRUTOS, J. C. 2020. Influence of Bone Definition and Finite Element Parameters in Bone and Dental Implants Stress: A Literature Review. *Biology (Basel),* 9.

PRASAD, J., WIATER, B. P., NORK, S. E., BAIN, S. D. & GROSS, T. S. 2010. Characterizing gait induced normal strains in a murine tibia cortical bone defect model. *J Biomech,* 43**,** 2765-70.

RAJAPAKSE, C. S., MAGLAND, J. F., WALD, M. J., LIU, X. S., ZHANG, X. H., GUO, X. E. & WEHRLI, F. W. 2010. Computational biomechanics of the distal tibia from high-resolution MR and micro-CT images. *Bone,* 47**,** 556-63.

RHO, J. Y., HOBATHO, M. C. & ASHMAN, R. B. 1995. Relations of mechanical properties to density and CT numbers in human bone. *Med Eng Phys,* 17**,** 347-55.

RICHMOND, J. 2002. Refinement, reduction, and replacement of animal use for regulatory testing: future improvements and implementation within the regulatory framework. *ILAR J,* 43 Suppl**,** S63-8.

ROGGE, R. D., ADAMS, B. D. & GOEL, V. K. 2002. An analysis of bone stresses and fixation stability using a finite element model of simulated distal radius fractures. *J Hand Surg Am,* 27**,** 86-92.

ROWE, D. W., ADAMS, D. J., HONG, S. H., ZHANG, C., SHIN, D. G., RENATA RYDZIK, C., CHEN, L., WU, Z., GARLAND, G., GODFREY, D. A., SUNDBERG, J. P. & ACKERT-BICKNELL, C. 2018. Screening Gene Knockout Mice for Variation in Bone Mass: Analysis by muCT and Histomorphometry. *Curr Osteoporos Rep,* 16**,** 77-94.

SAN-JULIAN, M., AQUERRETA, J. D., BENITO, A. & CANADELL, J. 1999. Indications for epiphyseal preservation in metaphyseal malignant bone tumors of children: relationship between image methods and histological findings. *J Pediatr Orthop,* 19**,** 543-8.

SARTORIUS, T., LUTZ, S. Z., HOENE, M., WAAK, J., PETER, A., WEIGERT, C., RAMMENSEE, H. G., KAHLE, P. J., HARING, H. U. & HENNIGE, A. M. 2012. Toll-like receptors 2 and 4 impair insulin-mediated brain activity by interleukin-6 and osteopontin and alter sleep architecture. *FASEB J,* 26**,** 1799-809.

SCHAPIRA, D. & SCHAPIRA, C. 1992. Osteoporosis: the evolution of a scientific term. *Osteoporos Int,* 2**,** 164-7.

SCHILEO, E. & TADDEI, F. 2021. Finite Element Assessment of Bone Fragility from Clinical Images. *Curr Osteoporos Rep,* 19**,** 688-698.

SCHILEO, E., TADDEI, F., MALANDRINO, A., CRISTOFOLINI, L. & VICECONTI, M. 2007. Subject-specific finite element models can accurately predict strain levels in long bones. *J Biomech,* 40**,** 2982-9.

SCHWARTZ, A. V., VITTINGHOFF, E., BAUER, D. C., HILLIER, T. A., STROTMEYER, E. S., ENSRUD, K. E., DONALDSON, M. G., CAULEY, J. A., HARRIS, T. B., KOSTER, A., WOMACK, C. R., PALERMO, L., BLACK, D. M., STUDY OF OSTEOPOROTIC FRACTURES RESEARCH, G., OSTEOPOROTIC FRACTURES IN MEN RESEARCH, G., HEALTH, A. & BODY COMPOSITION RESEARCH, G. 2011. Association of BMD and FRAX score with risk of fracture in older adults with type 2 diabetes. *JAMA,* 305**,** 2184-92.

SCHWARZENBERG, P. & DAILEY, H. L. 2020. Elementwise material assignment in reconstructed or transformed patient-specific FEA models developed from CT scans. *Comput Methods Biomech Biomed Engin,* 23**,** 92-102.

SEILER, I. 2017. *CCN4/WISP-1 Knockout Compromises Bone integrity in Mice.* B.Sc. Medizintechnik, Eberhard-Karls University Tübingen.

SHANMUGAVADIVU, A., BALAGANGADHARAN, K. & SELVAMURUGAN, N. 2022. Angiogenic and Osteogenic Effects of Flavonoids in Bone Regeneration.

Biotechnol Bioeng.

SHARIR, A., BARAK, M. M. & SHAHAR, R. 2008. Whole bone mechanics and mechanical testing. *Vet J,* 177**,** 8-17.

SILVA, M. J., BRODT, M. D., WOPENKA, B., THOMOPOULOS, S., WILLIAMS, D., WASSEN, M. H., KO, M., KUSANO, N. & BANK, R. A. 2006. Decreased collagen organization and content are associated with reduced strength of demineralized and intact bone in the SAMP6 mouse. *J Bone Miner Res,* 21**,** 78-88.

STEVENS, D. J. & LATORRACA, R. 1977. Monitoring heparin therapy. *Wis Med J,* 76**,** 33-6.

TAYLOR, K. & ALVAREZ, L. R. 2019. An Estimate of the Number of Animals Used for Scientific Purposes Worldwide in 2015. *Altern Lab Anim,* 47**,** 196-213.

TERZI, M. M., DESERNO, M. & NAGLE, J. F. 2019. Mechanical properties of lipid bilayers: a note on the Poisson ratio. *Soft Matter,* 15**,** 9085-9092.

TURNER, M. J., CLOUGH, R. W., C., M. H. & TOPP, L. J. 1965. Stiffness and Deflection Analysis of Complex Structures. *Journal of the Aeronautical Sciences,* 23**,** 805-823.

VAN RIETBERGEN, B., MAJUMDAR, S., NEWITT, D. & MACDONALD, B. 2002. High-resolution MRI and micro-FE for the evaluation of changes in bone mechanical properties during longitudinal clinical trials: application to calcaneal bone in postmenopausal women after one year of idoxifene treatment. *Clin Biomech (Bristol, Avon),* 17**,** 81-8.

VARGA, P., WILLIE, B. M., STEPHAN, C., KOZLOFF, K. M. & ZYSSET, P. K. 2020. Finite element analysis of bone strength in osteogenesis imperfecta. *Bone,* 133**,** 115250.

VICHNIN, H. H. & BATTERMAN, S. C. 1986. Stress analysis and failure prediction in the proximal femur before and after total hip replacement. *J Biomech Eng,* 108**,** 33-41.

VIERO, A., BIEHLER-GOMEZ, L., MESSINA, C., CAPPELLA, A., GIANNOUKOS, K., VIEL, G., TAGLIARO, F. & CATTANEO, C. 2022. Utility of micro-CT for dating post-cranial fractures of known post-traumatic ages through 3D measurements of the trabecular inner morphology. *Sci Rep,* 12**,** 10543.

VURTUR BADARINATH, P., CHIERICHETTI, M. & DAVOUDI KAKHKI, F. 2021. A Machine Learning Approach as a Surrogate for a Finite Element Analysis: Status of Research and Application to One Dimensional Systems. *Sensors (Basel),* 21.

WANG, J., ZHOU, B., LIU, X. S., FIELDS, A. J., SANYAL, A., SHI, X., ADAMS, M., KEAVENY, T. M. & GUO, X. E. 2015. Trabecular plates and rods determine elastic modulus and yield strength of human trabecular bone. *Bone,* 72**,** 71-80.

WOLFF, J. 1892. *Das Gesetz der Transformation der Knochen. Berlin: A. Hirchwild.*

XIN, P., NIE, P., JIANG, B., DENG, S., HU, G. & SHEN, S. G. 2013. Material assignment in finite element modeling: heterogeneous properties of the mandibular bone. *J Craniofac Surg,* 24**,** 405-10.

XU, Y., LI, X., CHANG, Y., WANG, Y., CHE, L., SHI, G., NIU, X., WANG, H., LI, X., HE, Y., PEI, B. & WEI, G. 2022. Design of Personalized Cervical Fixation Orthosis Based on 3D Printing Technology. *Appl Bionics Biomech,* 2022**,** 8243128.

YANG, Z., YI, P., LIU, Z., ZHANG, W., MEI, L., FENG, C., TU, C. & LI, Z. 2022. Stem Cell-Laden Hydrogel-Based 3D Bioprinting for Bone and Cartilage Tissue Engineering. *Front Bioeng Biotechnol,* 10**,** 865770.

YOUNG, S. A. E., RUMMLER, M., TAIEB, H. M., GARSKE, D. S., ELLINGHAUS, A., DUDA, G. N., WILLIE, B. M. & CIPITRIA, A. 2022. In vivo microCT-based time-lapse morphometry reveals anatomical site-specific differences in bone (re)modeling serving as baseline parameters to detect early pathological events. *Bone,* 161**,** 116432.

ZHANG, J. L., POON, C. C., WONG, M. S., LI, W. X., GUO, Y. X. & ZHANG, Y. 2022a. Vitamin D Supplementation Improves Handgrip Strength in Postmenopausal Women: A Systematic Review and Meta-Analysis of Randomized Controlled Trials. *Front Endocrinol (Lausanne),* 13**,** 863448.

ZHANG, P., YU, B., SHAO, S., ZHANG, R., ZENG, Y., LI, J., REN, C., ZHOU, X. & ZHAO, J. 2022b. Exploring the relationship of brown adipose tissue to bone microarchitecture using 7T MRI and micro-CT. *Histol Histopathol***,** 18481.

ZHU, X. Z., HAN, C. X., AI, Z. S., WANG, W., WU, S. H., ZHAO, K. Y., LIAO, P. & MEI, J. 2022. A quantitative study of bone defects in displaced femoral neck fractures based on virtual reduction techniques. *Comput Methods Programs Biomed,* 222**,** 106958.

ZIOUPOS, P., COOK, R. & COATS, A. M. 2008. Bone quality issues an matrix properties in OP cancellous bone. *Stud Health Technol Inform,* 133**,** 238-45.

9. Declaration

The research was conducted at Siegfried Weller Institute for Trauma Research, Eberhard Karls Universität Tübingen, Tübingen.

Prof. Dr. rer nat. Andreas K. Nüssler, PD Dr. sc hum. Sabrina Ehnert and I conceptualized the study. PD Dr. sc hum. Sabrina Ehnert and I conceived and designed the experiments. All experiments were carried out and analyzed by myself. I declare that all relevant data are our original work, except for the quoted data and references.

I hereby declare that the submitted thesis entitled: “The establishment of finite element models to characterize mechanical properties of mouse tibiae based on micro-CT data” has been written by myself. This work has not been submitted for any other degree.

_____

Place/date/signature of the doctoral candidate

10. Publication

The results of this thesis were partially used for publication:

- *Title:*

Contribution to the 3R principle: Description of a specimen-specific finite element model simulating 3-point-bending tests in mouse tibiae.

Author:

Xiaowei Huang, Andreas K. Nussler, Marie K. Reumann, Peter Augat, Maximilian M. Menger, Ahmed Ghallab, Jan G. Hengstler, Tina Histing, Sabrina Ehnert

Journal: Bioengineering (Basel) **2022**, *9*(8), 337.Impact score 5.046.

11. Acknowledgements

I would like to express my gratitude to the people who helped me a lot in completing the dissertation. First, I would like to thank Prof. Dr. Andreas K. Nüssler. I appreciate that Professor Nüssler allowed me to study in Germany and provided me with a lot of help, both in life and in the lab. Secondly, I am very grateful to PD Dr. sc hum. Sabrina Ehnert for her academic guidance. At her suggestion, I applied the finite element technique to the mouse tibia, which led to the creation of this MD dissertation. PD Dr. sc hum. Sabrina Ehnert is a very professional and experienced scientist. She taught me how to use story thinking for essay writing, which was a new experience. I am also very grateful for the technical support the technician Bianca Braun provided. She taught me cell culture techniques and PCR techniques. Her explanation is very detailed and professional, which helped me immensely in my experiment.

Apart from that, I would like to express my gratitude to Romina, Regina, Helen, Caren, and Svetlana for making my life in the lab much easier. At last, I also want to express my appreciation to my Chinese fellows, Shen, Liu, Lu, Weidong, and Yangmenfan, for giving me a lot of advice on life and experiments.